

Citation for published version:

Price, SH, Shimizu, TT, Genzel, R, Übler, H, Förster Schreiber, NM, Tacconi, LJ, Coogan, RT, Lutz, D, Wuyts, S, Wisnioski, E, Nestor, A, Sternberg, A, Burkert, A, Bender, R, Contursi, A, Herrera-camus, R, Lee, M, Naab, T, Neri, R, Renzini, A, Saglia, R, Schruba, A & Schuster, K 2021, 'Rotation Curves in $z = 1-2$ Star-forming Disks: Comparison of Dark Matter Fractions and Disk Properties for Different Fitting Methods', *The Astrophysical Journal*, vol. 922, no. 2, 143. <https://doi.org/10.3847/1538-4357/ac22ad>

DOI:

[10.3847/1538-4357/ac22ad](https://doi.org/10.3847/1538-4357/ac22ad)

Publication date:

2021

Document Version

Peer reviewed version

[Link to publication](#)

This is an author-created, un-copyedited version of an article published in The Astrophysical Journal. IOP Publishing Ltd is not responsible for any errors or omissions in this version of the manuscript or any version derived from it. The Version of Record is available online at <https://doi.org/10.3847/1538-4357/ac22ad>.

University of Bath

Alternative formats

If you require this document in an alternative format, please contact:
openaccess@bath.ac.uk

General rights

Copyright and moral rights for the publications made accessible in the public portal are retained by the authors and/or other copyright owners and it is a condition of accessing publications that users recognise and abide by the legal requirements associated with these rights.

Take down policy

If you believe that this document breaches copyright please contact us providing details, and we will remove access to the work immediately and investigate your claim.

Rotation Curves in $z \sim 1-2$ Star-Forming Disks: Comparison of Dark Matter Fractions and Disk Properties for Different Fitting Methods

S. H. PRICE,^{1,*} T. T. SHIMIZU,¹ R. GENZEL,^{1,2} H. ÜBLER,¹ N. M. FÖRSTER SCHREIBER,¹ L. J. TACCONI,¹ R. I. DAVIES,¹ R. T. COOGAN,¹
D. LUTZ,¹ S. WUYTS,³ E. WISNIOSKI,^{4,5} A. NESTOR,⁶ A. STERNBERG,^{1,6,7} A. BURKERT,^{1,8} R. BENDER,^{1,8} A. CONTURSI,^{1,9}
R. L. DAVIES,¹⁰ R. HERRERA-CAMUS,¹¹ M.-J. LEE,¹ T. NAAB,¹² R. NERI,⁹ A. RENZINI,¹³ R. SAGLIA,^{1,8} A. SCHRUBA,¹ AND
K. SCHUSTER⁹

¹Max-Planck-Institut für extraterrestrische Physik (MPE), Giessenbachstr. 1, D-85748 Garching, Germany

²Departments of Physics and Astronomy, University of California, Berkeley, CA 94720, USA

³Department of Physics, University of Bath, Claverton Down, Bath BA2 7AY, UK

⁴Research School of Astronomy and Astrophysics, Australian National University, Canberra, ACT 2611, Australia

⁵ARC Centre of Excellence for All Sky Astrophysics in 3 Dimensions (ASTRO 3D), Australia

⁶School of Physics and Astronomy, Tel Aviv University, Tel Aviv 69978, Israel

⁷Center for Computational Astrophysics, Flatiron Institute, 162 5th Avenue, New York, NY 10010, USA

⁸Universitäts-Sternwarte Ludwig-Maximilians-Universität (USM), Scheinerstr. 1, D-81679 München, Germany

⁹Institute for Radio Astronomy in the Millimeter Range (IRAM), Rue de la Piscine, Grenoble, France

¹⁰Centre for Astrophysics and Supercomputing, Swinburne University of Technology, John St, Hawthorn VIC 3122, Australia

¹¹Astronomy Department, Universidad de Concepción, Av. Esteban Iturra s/n Barrio Universitario, Casilla 160, Concepción, Chile

¹²Max-Planck-Institut für Astrophysik (MPA), Karl Schwarzschildstr. 1, D-85748 Garching, Germany

¹³INAF - Osservatorio Astronomico di Padova, Vicolo dell'Osservatorio 5, I-35122 Padova, Italy

ABSTRACT

We present a follow-up analysis examining the dynamics and structures of 41 massive, large star-forming galaxies at $z \sim 0.67-2.45$ using both ionized and molecular gas kinematics. We fit the galaxy dynamics with models consisting of a bulge, a thick, turbulent disk, and a NFW dark matter halo, using code that fully forward models the kinematics, including all observational and instrumental effects. We explore the parameter space using Markov Chain Monte Carlo (MCMC) sampling, including priors based on stellar and gas masses and disk sizes. We fit the full sample using extracted 1D kinematic profiles. For a subset of 14 well-resolved galaxies, we also fit the 2D kinematics. The MCMC approach robustly confirms the results from least-squares fitting presented in [Paper I](#) (Genzel et al. 2020): the sample galaxies tend to be baryon-rich on galactic scales (within one effective radius). The 1D and 2D MCMC results are also in good agreement for the subset, demonstrating that much of the galaxy dynamical information is captured along the major axis. The 2D kinematics are more affected by the presence of non-circular motions, which we illustrate by constructing a toy model with constant inflow for one galaxy that exhibits residual signatures consistent with radial motions. This analysis, together with results from [Paper I](#) and other studies, strengthens the finding that massive, star-forming galaxies at $z \sim 1-2$ are baryon-dominated on galactic scales, with lower dark matter fractions towards higher baryonic surface densities. Finally, we present details of the kinematic fitting code used in this analysis.

Keywords: galaxies: kinematics and dynamics — galaxies: structure — galaxies: high-redshift

1. INTRODUCTION

Galaxy kinematics are a key probe of galaxy structure and mass distribution, as they provide a direct trace of the mass distribution that is not directly affected by dust attenuation or uncertainties in estimates of stellar or gas masses (van der Kruit & Allen 1978, van der Kruit & Freeman 2011, Courteau et al. 2014). Kinematic measurements can therefore be used to probe the amount of dark matter on galactic scales. Numerous studies over several decades have used kinematics

to constrain the detailed mass distributions of nearby galaxies and their dark matter halos (including Rubin & Ford, W. Kent 1970, Freeman 1970, Casertano 1983, Carignan & Freeman 1985, van Albada et al. 1985, and many others). In the local Universe, galaxy dynamics can be probed with stellar spectroscopy and a wide range of gas tracers, including ionized, neutral, and molecular gas ($H\alpha$, HI, and CO). For star-forming galaxies (SFGs), the gas tracers can often be used past the galaxies' optical extent (e.g. Courteau et al. 2014, and references therein). Put together, kinematic measurements using all available tracers provide detailed constraints on local galaxies' mass distributions and dynamics, which tell us

* Email: sedona@mpe.mpg.de

not only about the galaxies’ present state, but also about how they formed.

Observations of galaxy kinematics at multiple epochs over cosmic time provide a powerful probe of the evolution of galactic structure, and of the relative amount and distribution of baryons versus dark matter. With the advent of sensitive near-infrared (near-IR) integral field unit (IFU) and slit spectrographs on 8-10m telescopes, ionized gas kinematics from strong rest-frame optical emission lines, in particular $H\alpha$, have become routinely accessible at $z \sim 1-3$. Dynamical masses (M_{dyn}) have been obtained for large samples of star-forming galaxies (SFGs) based on velocity and dispersion profiles in the central brighter regions, typically within the effective radius R_e , near the peak of the rotation curve for an exponential disk ($R_{\text{peak}} \sim 1.3R_e$). Several studies comparing M_{dyn} estimates with stellar masses derived from multi-band photometry and gas masses obtained from observations of cold molecular gas/dust or inferred from scaling relations, have indicated that in these inner regions, $z \sim 2$ SFGs have comparable or higher baryonic mass fractions than local disks of similar masses (e.g., Förster Schreiber et al. 2006, 2009, Erb et al. 2006, Price et al. 2016, 2020, Wuyts et al. 2016).

Ideally, measurements should probe kinematics further out, well beyond $\sim 1-1.5R_e$ for two main reasons. Firstly, one can then use the *shape* of the rotation curve (RC) to constrain the mass distribution, alleviating the large uncertainties associated with light-to-mass conversions in computing stellar (M_*) and gas masses (M_{gas}). Secondly, the decomposition into baryonic and dark matter mass components is more robust when the range of radii probe from inner regions where baryons dominate into regions where the relative contribution of dark matter becomes more important. This requires very sensitive observations as the line emission from the galaxies gets very faint (e.g., exponential decrease of surface brightness with increasing radius for a disk with Sérsic index $n_S = 1$). Recent work capitalized on subsets with very deep data of individual galaxies, typically larger and/or with shallower light profile ($n_S \lesssim 1$) than average, i.e. with measurable emission extending further into the (inner) dark matter halo (e.g., Genzel et al. 2017, 2020, Drew et al. 2018, Übler et al. 2018, Molina et al. 2019). Other studies employed stacking techniques to derive the average RC of larger numbers of galaxies (Lang et al. 2017, Tiley et al. 2019). In yet another approach, van Dokkum et al. (2015) constructed a composite RC, inferring rotation velocities from integrated line widths of a dozen compact and high-mass SFGs. Modeling of these individual or stacked RCs showed most robustly that $z \sim 1-3$ SFGs tend to be strongly baryon-dominated on galactic scales (Genzel et al. 2017, Lang et al. 2017, Übler et al. 2018), although these findings were challenged by Tiley et al. (2019), who favored a different RC normalization scheme than Lang et al. (2017) in their stacking approach. Mixed results in the literature likely reflect a combination of differences in methodologies and modeling, together with genuine trends among the galaxy population (e.g., see discussion by Förster Schreiber & Wuyts 2020).

Modeling high-quality, individual extended $H\alpha$ or CO RCs of 41 $z \sim 0.67-2.45$ SFGs, Genzel et al. (2020) recently confirmed the baryon dominance in a majority of these galaxies and also revealed important underlying trends, with $f_{\text{DM}}(R_e)$ anticorrelating most strongly with central mass surface density, bulge mass M_{bulge} , and angular momentum parameter. These results echo trends highlighted from inner disk kinematics by Wuyts et al. (2016) and seen in recent high-resolution numerical simulations of galaxy evolution (Lovell et al. 2018, Teklu et al. 2018, Übler et al. 2021). As shown by Genzel et al. (2020), low dark matter fractions on $\sim 1R_e$ scales can be explained by shallower inner dark matter mass distributions than “NFW” profiles (Navarro et al. 1996), possibly due to heating by dynamical friction of satellites and AGN feedback. The results are also consistent with efficient radial transport in gas-rich environments at high redshift, leading to the rapid buildup of massive bulges and central black holes.

In this paper, we follow-up on Genzel et al. (2020) (from here on, Paper I) by assessing the impact of fitting approach and of kinematic modeling in 1D versus 2D. We model the same RCs of all 41 galaxies via a Markov Chain Monte Carlo (MCMC) technique to compare to the least-squares minimization adopted in Paper I. For a subset of 14 SFGs with deep adaptive optics-assisted IFU data, we further compare the results from modeling the 1D major-axis kinematic profiles to modeling the full 2D kinematic maps. Our analysis demonstrates the robustness of the findings of high baryonic fractions on galactic scales, and shows that the information about the overall mass distribution is well captured in the 1D major-axis profiles for these disk galaxies. We further highlight the potential of second-order deviations from axisymmetric rotation in probing the processes, such as radial inflows, that may efficiently concentrate baryons within the inner galactic regions at early $z \sim 1-3$ epochs. We also present the details of the updated version of the galaxy kinematics modeling code `DysmaLpY`.

Throughout, we assume a Λ CDM cosmology with $\Omega_m = 0.3$, $\Omega_\Lambda = 0.7$, and $H_0 = 70 \text{ km s}^{-1} \text{ Mpc}^{-1}$, and a Chabrier (2003) initial mass function.

2. SAMPLE AND DATA

The RC41 sample consists of 41 individual star-forming and kinematically-classified disk galaxies at redshifts $z = 0.65-2.45$. As shown in Figure 1 of Paper I, these galaxies range in stellar mass and size from $\log_{10}(M_*/M_\odot) \sim 9.8-11.4$ and $R_e \sim 2.5-10 \text{ kpc}$ (the projected major-axis half-light radius from stellar rest-frame 5000\AA light). The galaxies lie near the SFR versus M_* “main sequence” of SFGs (MS; e.g., Speagle et al. 2014, Whitaker et al. 2014), and tend to be larger than average at their stellar mass and redshift (based on the mass-size relationship of van der Wel et al. 2014). The size bias results mainly from the selection of galaxies with sufficiently well-resolved data and the most extended kinematic profiles to enable analysis of the outer disk RCs (i.e. beyond $\sim 1-1.5R_e$).

Table 1. General Galaxy Parameters^a

ID	z	$\log_{10}(M_*/M_{\odot})_{\text{SED}}$	SFR	$\log_{10}(M_{\text{gas}}/M_{\odot})^b$	B/T	$R_{e,\text{disk}}^c$	$n_{S,\text{disk}}$	$q_{0,\text{disk}}$	i	c_{halo}
		[dex]	[$M_{\odot} \text{ yr}^{-1}$]	[dex]	—	[kpc]	—	—	[deg]	—
EGS3_10098	0.658	11.11	52.0	10.50	0.60	3.0	1.0	0.14	31.0	7.3
U3_21388	0.669	10.76	4.8	10.01	0.05	7.0	1.0	0.14	82.0	7.2
EGS4_21351	0.732	10.94	79.5	10.60	0.46	3.3	1.0	0.15	47.0	6.8
EGS4_11261	0.748	11.25	85.0	10.76	0.50	4.0	1.0	0.10	59.7	6.6
GS4_13143	0.760	9.82	12.0	9.82	0.70	5.6	1.3	0.15	74.0	6.5
U3_05138	0.809	10.20	6.0	9.88	0.50	7.5	1.0	0.12	55.0	6.5
GS4_03228	0.824	9.49	10.1	9.69	0.80	7.0	1.0	0.15	78.0	6.5
GS4_32976	0.831	10.37	22.0	10.19	0.90	6.8	1.0	0.17	68.0	6.5
COS4_01351	0.854	10.73	57.0	10.58	0.24	8.0	0.9	0.15	68.0	6.5
COS3_22796	0.914	10.32	11.1	10.10	0.15	9.0	1.0	0.17	58.0	6.1
U3_15226	0.922	11.11	31.0	10.54	0.55	5.5	1.0	0.17	50.0	6.1
GS4_05881	0.990	9.78	19.0	9.92	0.85	5.6	1.3	0.17	60.0	6.0
COS3_16954	1.031	10.74	100.0	10.72	0.50	8.1	1.0	0.17	49.5	6.1
COS3_04796	1.032	10.80	51.0	10.63	0.18	9.7	1.1	0.10	50.0	6.1
EGS_13035123	1.120	11.18	126.0	10.95	0.20	10.2	1.0	0.17	24.0	6.0
EGS_13004291	1.197	10.97	630.0	11.54	0.61	3.0	1.3	0.17	27.0	6.0
EGS_13003805	1.232	11.23	200.0	11.32	0.29	5.6	1.2	0.17	37.0	5.9
EGS4_38153	1.362	10.44	78.0	10.55	0.16	5.9	1.0	0.20	75.0	5.0
EGS4_24985	1.400	10.90	99.0	10.70	0.40	4.6	1.0	0.20	40.0	5.0
zC_403741	1.446	10.65	60.0	10.45	0.68	2.6	1.0	0.20	28.0	5.0
D3a_6397	1.500	11.08	214.0	11.00	0.57	6.3	1.0	0.24	30.0	5.0
EGS_13011166	1.530	11.08	375.0	11.41	0.55	6.3	1.0	0.20	60.0	5.0
GS4_43501	1.614	10.61	53.0	10.51	0.40	4.9	0.6	0.20	62.0	5.0
GS4_14152	1.615	11.30	167.0	11.07	0.23	6.8	1.0	0.20	55.0	5.0
K20_ID9	2.036	10.65	81.0	10.66	0.30	7.1	1.0	0.25	48.0	4.0
zC_405501	2.154	9.92	60.0	10.27	0.07	5.0	0.2	0.25	75.0	4.0
SSA22_MD41	2.172	9.86	130.0	10.46	0.05	7.1	0.4	0.25	72.0	4.0
BX389	2.180	10.60	100.0	10.68	0.30	7.4	0.2	0.25	76.0	4.0
zC_407302	2.182	10.39	340.0	10.60	0.50	4.0	1.0	0.12	60.0	4.0
GS3_24273	2.187	11.00	267.0	11.03	0.80	7.0	1.0	0.25	60.0	4.0
zC_406690	2.196	10.62	300.0	10.91	0.90	4.5	0.2	0.25	25.0	4.0
BX610	2.210	11.00	60.0	11.36	0.42	4.9	1.0	0.25	39.0	4.0
K20_ID7	2.225	10.28	101.0	10.59	0.03	8.2	0.2	0.25	64.0	4.0
K20_ID6	2.236	10.43	99.0	10.57	0.30	5.0	0.5	0.25	31.0	4.0
zC_400569	2.242	11.08	240.0	11.30	0.70	4.0	1.0	0.22	45.0	4.0
BX482	2.258	10.26	80.0	10.91	0.02	5.8	0.2	0.25	60.0	4.0
COS4_02672	2.308	10.57	72.0	10.61	0.10	7.4	0.5	0.25	62.0	4.0
D3a_15504	2.383	11.04	146.0	10.92	0.30	6.1	1.0	0.25	40.0	4.0
D3a_6004	2.387	11.50	355.0	11.27	0.44	5.3	0.4	0.25	20.0	4.0
GS4_37124	2.431	10.59	194.0	10.70	0.70	3.2	1.0	0.25	67.0	4.0
GS4_42930	2.451	10.33	70.0	10.37	0.50	2.8	1.2	0.25	59.0	4.0

^a Parameters include redshift (z), stellar mass (M_*), SFR, gas mass (M_{gas}), bulge-to-total ratio (B/T), the effective radius ($R_{e,\text{disk}}$), Sérsic index ($n_{S,\text{disk}}$), and intrinsic axis ratio ($q_{0,\text{disk}}$) of the disk, inclination (i), and halo concentration (c_{halo}).

^b From direct measurements, or gas-mass scaling relations.

^c Best-fit $R_{e,\text{disk}}$ from Paper I.

The kinematic data are drawn from observations of ionized gas (traced with $\text{H}\alpha$) and cold molecular gas (traced with CO). The data come from near infrared observations with SINFONI (IFU, in both seeing-limited and adaptive optics-assisted modes) and KMOS (IFU, seeing-limited) at ESO/VLT, and with LBT-LUCI (slit, seeing-limited), together with millimeter interferometry from IRAM/NOEMA. The observations for each galaxy probe out to $\sim 1.5-4$ times the effective radius, which is crucial for detailed kinematic modeling. The median on-source integration time is 16 hours,

with individual data sets ranging from 4 to 56 hours. Table 1 lists the basic properties of the sample, including z , M_* , SFR, gas mass, and structural parameters, as well as the halo concentration parameter (adopted as a function of z only, based on the average of relations by Bullock et al. 2001, Dutton & Macciò 2014, Ludlow et al. 2014; see Tables 1, D1, D2 and Sec. 2 and Appendix A of Paper I for full details).

Most of the information about the underlying mass distribution of disks is expected to be encoded in the velocity and velocity dispersion profiles along the projected kinematic ma-

major axis (c.f., Genzel et al. 2006, 2017; see also Section 5). For the comparison of fitting methodology, we use the same 1D profiles as in Paper I, where details of their extraction can be found. In summary, except for the LBT/LUCI slit spectroscopic H α data of two objects, the profiles were obtained from the H α or CO data cubes using a pseudo-slit along the kinematic major axis. The pseudo-slit width is either constant and ~ 1 –1.5 times the point-spread function full-width at half-maximum (PSF FWHM), or increasing towards the outskirts for more face-on galaxies (with opening angle ~ 5 –10 degrees). This choice of slit width and geometry best samples the major-axis kinematics given the projected isovelocity contours of inclined disks, maximizing the S/N and radial extent while minimizing contamination of signal away from the major axis. For galaxies with IFU observations in more than one mode (seeing-limited or AO-assisted) or more than one instrument (SINFONI + KMOS), the data are combined into a composite cube before performing the 1D extraction. For EGS4-24985 and EGS-13011166, observed with LBT/LUCI and with NOEMA, the independently extracted 1D profiles are combined together (see also Genzel et al. 2013, Übler et al. 2018).

For the subset of galaxies with AO observations, we also extract 2D velocity and dispersion maps. As most of these objects also have seeing-limited observations, we extract maps from the cubes combining the AO and non-AO H α data in order to maximize the S/N and radial coverage. For the composite cubes, uncertainties are estimated using RMS flux variations in the spectral ranges free from emission lines. We then use LINEFIT to measure the 2D kinematic maps from the composite cubes (Förster Schreiber et al. 2009, 2018, Davies et al. 2011). The velocity and dispersion maps (corrected for instrumental spectral resolution) are obtained by fitting a Gaussian to the H α line in the spectrum of each spaxel, after spectral and spatial median-filtering of the input data cube by 3 pixels in each dimension (similar to the resolution element, to mitigate noise peaks). Uncertainties are derived through a Monte Carlo approach, by perturbing the input spectrum 100 times according to the noise cube associated with each data cube and assuming a Gaussian noise distribution. Masks for the 2D maps are created using a combination of criteria. These include an integrated line flux S/N cut (generally $\gtrsim 5\sigma$), together with (where necessary) an integrated line flux fraction cut ($\gtrsim 0.05$ – $0.1 f_{\max}$). We also use fit uncertainty cuts for both the velocity and dispersion maps (typically $\gtrsim 3$ – 5σ) as well as sigma clipping of the kinematics as needed (mostly $\gtrsim 3$ – 5σ). Segmentation maps are also incorporated to detangle the flux from e.g. neighboring bright clumps. We additionally flag a small number of outlier pixels not otherwise excluded, or explicitly include a few non-problematic lower flux pixels falling within otherwise unmasked regions. In order to have the highest possible spatial resolution, when examining features in residual maps we additionally consider only the AO data (see Section 5.2).

3. DYNAMICAL MODELING

To model the kinematics of the galaxies, we employ the fully 3D code DYSMAL, which has been continually optimized for applications to high redshift studies (Genzel et al. 2006, 2011, 2014, 2017, 2020, Cresci et al. 2009, Davies et al. 2011, Wuyts et al. 2016, Lang et al. 2017, Übler et al. 2018). The code is parametric, and follows a forward modeling approach, incorporating one or more mass and kinematic components and accounting for all observational effects (such as projection, beam smearing, etc.). The fits to 1D and 2D measurements use profiles and maps from the 3D model cube extracted in a similar way as for the observations. The latest DYSMAL upgrade in functionality and model ingredients is presented in Appendix A. In this section, we give the specific model choices used for the present analysis.

3.1. Galaxy Model Components

As in Paper I, we model each galaxy as a thick, turbulent disk and a bulge embedded in a dark matter halo, adopting the same treatment and assumptions. The disk and bulge components are modeled as deprojected Sérsic profiles, following Noordermeer (2008). We assume the bulge is spherical, with index $n_{S,\text{bulge}} = 4$ and projected effective radius $R_{e,\text{bulge}} = 1$ kpc. The disk is taken to be an oblate, flattened spheroid with intrinsic axis ratio $q_{0,\text{disk}}$, index $n_{S,\text{disk}}$, and radius $R_{e,\text{disk}}$. The masses of the disk and bulge components are calculated based on the total baryonic mass, $\log_{10}(M_{\text{bar}}/M_{\odot})$, and the bulge-to-total ratio, B/T . The circular velocity curve for the disk and bulge are then calculated using Eq. 10 of Noordermeer (2008). Following the approach in Paper I for consistency, we assume that only the disk component contributes to the light of our tracer (H α or CO), and that the disk light distribution follows a Sérsic profile.

Our model also includes a dark matter halo with a NFW profile (Navarro et al. 1996), to provide the most direct comparison to the least-squares analysis in Paper I. The halo has a mass M_{vir} and fixed concentration c_{halo} , which is adopted based on the typical redshift evolution of dark matter halo concentrations (e.g., Bullock et al. 2001, Dutton & Macciò 2014, Moster et al. 2020). For this analysis, we do not include any halo adiabatic contraction.

We assume the intrinsic velocity dispersion of our galaxies is constant and isotropic throughout the disk, with value σ_0 . The corresponding pressure support — important for the dynamics of thick disks — is accounted for by applying an asymmetric drift correction to the model circular velocity v_{circ} in computing the actual rotation velocity v_{rot} following the relation presented by Burkert et al. (2010) for exponential disks (their Eq. 11; see also Eq. A4).

3.2. Fitting 1D Kinematic Profiles

The best-fit modeling parameters in Paper I were derived from least-squares optimization, using boundaries on the free parameters that are based on stellar, gas, and morphological

Table 2. Priors for 1D MCMC Fitting

Parameter	Prior	Bounds
$\log_{10}(M_{\text{bar}}/M_{\odot})$	Gaus($\log_{10}(M_{*,\text{SED}} + M_{\text{gas}})$, 0.2 dex) ^a	[9, 13] dex
$f_{\text{DM}}(R_e)$	Flat	[0, 1]
σ_0	Flat	[5, 300] km s ⁻¹
$R_{e,\text{disk}}$	Gaus($R_{e,\text{disk}}^0$, 2 kpc) ^b	[1, 15] kpc

^a $\log_{10}(M_{*}/M_{\odot})_{\text{SED}}$ and $\log_{10}(M_{\text{gas}}/M_{\odot})$ are listed in Table 1.

^b The adopted values of $R_{e,\text{disk}}^0$ are given in Table 1.

properties. Here we instead use a MCMC parameter space exploration to determine the best-fit parameter values, following the general procedure described in Appendix A.2. The key difference is that the best-fit values for Paper I are determined using χ^2 minimization (i.e., maximizing the model likelihood given the data),¹ while for this analysis we use the MCMC-derived posterior distributions to determine best-fit values (i.e., combining the prior and likelihood information).

In this analysis, we simultaneously fit the 1D velocity and dispersion profiles for 4 free parameters: the log total baryonic mass, $\log_{10}(M_{\text{bar}}/M_{\odot})$; the disk effective radius, $R_{e,\text{disk}}$; the intrinsic velocity dispersion, σ_0 ; and the enclosed dark matter fraction $f_{\text{DM}}(R_e) = v_{\text{circ,DM}}^2(R_e)/v_{\text{circ,tot}}^2(R_e)$ (where here $R_e = R_{e,\text{disk}}$ ²). We assume Gaussian priors for $\log_{10}(M_{\text{bar}}/M_{\odot})$ with a standard deviation of 0.2 dex that are centered on the baryonic mass derived using $\log_{10}(M_{*}/M_{\odot})$ from SED fitting and either a direct measurement of $\log_{10}(M_{\text{gas}}/M_{\odot})$ (from Tacconi et al. 2013, 2018, and Freundlich et al. 2019) or an estimate using the scaling relations from Tacconi et al. (2020). We also bound the values within $\log_{10}(M_{\text{bar}}/M_{\odot}) \in [9, 13]$ dex. For $R_{e,\text{disk}}$, we adopt Gaussian priors of standard deviation 2 kpc that are centered on the fit value of $R_{e,\text{disk}}$ from Paper I,³ and also bound $R_{e,\text{disk}} \in [1, 15]$ kpc. Finally, we adopt flat bounded priors for the intrinsic dispersion ($\sigma_0 \in [5, 300]$ km s⁻¹) and dark matter fraction ($f_{\text{DM}}(R_e) \in [0, 1]$). For reference, the priors adopted for the 1D fitting are summarized in Table 2.

The remaining model parameters are fixed, as it is difficult to simultaneously fit for more parameters given the spatial resolution and S/N of the data. We adopt the values of $n_{S,\text{disk}}$, halo concentration c_{halo} , and the disk flattening $q_{0,\text{disk}}$ used in Paper I (see Tables D1 & D2). We also use the final values of inclination i and B/T from Paper I (determined from a combination of kinematic and imaging information), because estimates of inclination or B/T based only on imaging may

also suffer from the effects of attenuation or mass-to-light gradients. The model position angle PA is set to the measured kinematic major axis PA (as in Paper I; very similar to the rest-frame optical morphological PA). As the 1D velocity and dispersion profiles have been centered spatially and corrected for any systemic velocity, we fix $x_0 = y_0 = V_{\text{sys}} = 0$.

For the 1D fits, the MCMC chain sampling is run using 1000 walkers, with 200 steps after a burn-in of 50 steps. With these settings, the chains for all fits over all objects have a final mean acceptance fraction between 0.2 and 0.5. We then adopt the *maximum a posteriori* (MAP) values of the fit parameters as the best-fit values, where we jointly analyze the posteriors for the free-parameter priors (to account for degeneracies in the posterior distributions). The lower and upper 1σ uncertainties are then determined from the shortest interval containing 68% of the marginalized posterior for each parameter (as discussed in Appendix A.2). The best-fit MAP values for the 1D MCMC fitting are listed in Table 3.

3.3. Fitting 2D Kinematic Maps

For the 2D modeling of the sensitive, deepest-possible data (composite or AO-only), we also simultaneously fit the velocity and dispersion maps. We begin with the same model setup as for the 1D fits, but additionally allow the systemic velocity V_{sys} to vary. We fix the kinematic major axis position angle, inclination, and spatial center for the 2D fits, as asymmetries or non-circular motions in the 2D maps can impact these parameters. For the 2D fits, the MCMC sampling is also run with 1000 walkers, but the chains are run longer than for the 1D fitting. We adopt fiducial settings of 300 steps after a burn-in of 100 steps, but some objects require longer burn-in periods. For some objects, $R_{e,\text{disk}}$ is poorly constrained, so the 2D fits are repeated while fixing $R_{e,\text{disk}}$ to the best-fit values from the 1D MCMC fitting (given in Table 3). The priors used for the 2D fitting, and whether $R_{e,\text{disk}}$ is fixed or free, are listed in Table 4.

4. COMPARISON OF 1D KINEMATIC DISK FITTING USING LEAST-SQUARES AND MCMC

In Figure 1, we compare the best-fit values of the dark matter fraction $f_{\text{DM}}(R_e)$, baryonic mass $\log_{10}(M_{\text{bar}}/M_{\odot})$, intrinsic dispersion σ_0 , and disk effective radius $R_{e,\text{disk}}$ from Paper I and this analysis. We stress that both analyses are based on the same 1D observed rotation and dispersion profiles. Overall, we find fairly good agreement between the two fitting methodologies, with the MCMC results finding the same overall trends and results as in Paper I.

The MCMC analysis tends to find slightly higher dark matter fractions, with a median offset of $\langle \Delta f_{\text{DM}}(R_e) \rangle = \langle f_{\text{DM}}(R_e)_{\text{MCMC}} - f_{\text{DM}}(R_e)_{\text{least-sq.}} \rangle = 0.12$ between the analyses. We also find correspondingly slightly lower baryonic masses than the least-squares analysis, with $\langle \Delta \log_{10}(M_{\text{bar}}/M_{\odot}) \rangle = -0.04$ dex. The derived velocity dispersions also tend to be higher in the MCMC, with

¹ The Paper I $f_{\text{DM}}(R_e)$ uncertainties are derived from a comparable MCMC fit (i.e., same free parameters), as MCMC sampling can efficiently and robustly capture multidimensional uncertainties (see Paper I, Appendix A.4).

² See also the discussion in Appendix A.3 for the choice of fitting parameter and effective priors on quantities inferred from fitted parameters, in particular the choice of fitting $f_{\text{DM}}(R_e)$ versus $\log_{10}(M_{\text{vir}}/M_{\odot})$.

³ While this prior choice is not independent from our data, it does allow us to include more information than just morphological fitting to imaging.

Table 3. Best-fit Parameters, 1D Fitting^a

ID	z	$\log_{10}(M_{\text{bar}}/M_{\odot})$	R_e	σ_0	$f_{\text{DM}}(R_e)$	$\log_{10}(M_{\text{vir}}/M_{\odot})^b$
		[dex]	[kpc]	[km s ⁻¹]	—	[dex]
		[Free]	[Free]	[Free]	[Free]	[Inferred]
EGS3_10098	0.658	10.93 ^{+0.11} _{-0.13}	3.93 ^{+1.95} _{-1.18}	61.70 ^{+9.99} _{-15.07}	0.27 ^{+0.13} _{-0.22}	12.55 ^{+1.21} _{-0.72}
U3_21388	0.669	10.80 ^{+0.17} _{-0.19}	8.68 ^{+1.52} _{-1.42}	51.04 ^{+7.78} _{-6.88}	0.69 ^{+0.13} _{-0.09}	12.72 ^{+0.22} _{-0.16}
EGS4_21351	0.732	10.68 ^{+0.07} _{-0.14}	5.90 ^{+1.71} _{-1.52}	30.00 ^{+7.01} _{-6.27}	0.11 ^{+0.13} _{-0.11}	10.53 ^{+1.26} _{-0.56}
EGS4_11261	0.748	11.11 ^{+0.20} _{-0.07}	5.49 ^{+2.75} _{-1.33}	41.34 ^{+8.46} _{-11.22}	0.24 ^{+0.11} _{-0.14}	12.52 ^{+0.78} _{-0.70}
GS4_13143	0.760	10.25 ^{+0.15} _{-0.10}	5.27 ^{+1.92} _{-1.31}	21.70 ^{+6.37} _{-8.06}	0.48 ^{+0.13} _{-0.13}	11.75 ^{+0.26} _{-0.26}
U3_05138	0.809	10.41 ^{+0.12} _{-0.12}	7.57 ^{+2.06} _{-1.54}	16.88 ^{+3.79} _{-9.41}	0.45 ^{+0.21} _{-0.16}	11.34 ^{+0.49} _{-0.33}
GS4_03228	0.824	9.98 ^{+0.19} _{-0.14}	6.76 ^{+1.76} _{-2.01}	13.88 ^{+3.83} _{-8.58}	0.75 ^{+0.11} _{-0.12}	11.88 ^{+0.20} _{-0.16}
GS4_32976	0.831	10.71 ^{+0.14} _{-0.18}	9.40 ^{+2.44} _{-2.63}	40.53 ^{+6.53} _{-9.70}	0.62 ^{+0.08} _{-0.10}	12.52 ^{+0.26} _{-0.25}
COS4_01351	0.854	10.97 ^{+0.18} _{-0.09}	7.08 ^{+2.63} _{-1.04}	63.67 ^{+5.09} _{-4.96}	0.53 ^{+0.11} _{-0.09}	12.87 ^{+0.23} _{-0.26}
COS3_22796	0.914	10.54 ^{+0.18} _{-0.15}	9.56 ^{+1.50} _{-2.01}	11.00 ^{+6.74} _{-5.92}	0.58 ^{+0.20} _{-0.18}	11.57 ^{+0.38} _{-0.33}
U3_15226	0.922	10.67 ^{+0.15} _{-0.09}	6.65 ^{+2.52} _{-1.47}	42.19 ^{+5.26} _{-7.87}	0.42 ^{+0.10} _{-0.16}	11.96 ^{+0.33} _{-0.43}
GS4_05881	0.990	10.13 ^{+0.13} _{-0.12}	4.71 ^{+2.31} _{-1.79}	63.48 ^{+5.11} _{-6.60}	0.76 ^{+0.12} _{-0.07}	12.92 ^{+0.18} _{-0.32}
COS3_16954	1.031	10.87 ^{+0.13} _{-0.09}	8.20 ^{+2.21} _{-1.33}	55.10 ^{+5.29} _{-7.23}	0.63 ^{+0.12} _{-0.10}	12.90 ^{+0.21} _{-0.22}
COS3_04796	1.032	11.12 ^{+0.14} _{-0.09}	9.22 ^{+2.18} _{-1.44}	18.82 ^{+2.48} _{-10.80}	0.49 ^{+0.12} _{-0.16}	12.54 ^{+0.27} _{-0.34}
EGS_13035123	1.120	11.09 ^{+0.09} _{-0.09}	10.17 ^{+1.92} _{-1.73}	19.33 ^{+2.09} _{-1.89}	0.28 ^{+0.15} _{-0.16}	11.45 ^{+0.56} _{-0.42}
EGS_13004291	1.197	11.12 ^{+0.05} _{-0.08}	4.48 ^{+2.15} _{-0.87}	59.34 ^{+8.83} _{-5.26}	0.08 ^{+0.16} _{-0.08}	11.35 ^{+1.66} _{-0.06}
EGS_13003805	1.232	11.43 ^{+0.09} _{-0.11}	6.70 ^{+1.61} _{-1.76}	40.45 ^{+9.86} _{-10.15}	0.18 ^{+0.09} _{-0.17}	12.19 ^{+1.08} _{-0.55}
EGS4_38153	1.362	10.94 ^{+0.17} _{-0.20}	4.17 ^{+1.91} _{-1.36}	58.48 ^{+8.70} _{-17.44}	0.47 ^{+0.20} _{-0.15}	13.50 ^{+0.38} _{-0.25}
EGS4_24985	1.400	11.14 ^{+0.12} _{-0.13}	5.94 ^{+1.39} _{-1.40}	43.03 ^{+7.25} _{-27.70}	0.35 ^{+0.17} _{-0.16}	12.83 ^{+0.50} _{-0.44}
zC_403741	1.446	10.60 ^{+0.04} _{-0.10}	3.28 ^{+2.27} _{-0.67}	69.48 ^{+6.27} _{-8.08}	0.05 ^{+0.18} _{-0.05}	10.29 ^{+1.86} _{-0.07}
D3a_6397	1.500	11.13 ^{+0.08} _{-0.07}	6.83 ^{+1.96} _{-1.68}	82.52 ^{+7.17} _{-11.02}	0.38 ^{+0.14} _{-0.17}	12.70 ^{+0.54} _{-0.46}
EGS_13011166	1.530	11.25 ^{+0.11} _{-0.08}	7.80 ^{+2.05} _{-1.42}	60.93 ^{+7.61} _{-8.67}	0.34 ^{+0.12} _{-0.10}	12.53 ^{+0.44} _{-0.33}
GS4_43501	1.614	10.82 ^{+0.16} _{-0.11}	5.05 ^{+2.15} _{-1.28}	46.04 ^{+5.16} _{-8.45}	0.38 ^{+0.12} _{-0.10}	12.31 ^{+0.37} _{-0.27}
GS4_14152	1.615	11.45 ^{+0.13} _{-0.10}	7.35 ^{+1.69} _{-1.67}	45.53 ^{+8.12} _{-11.61}	0.30 ^{+0.13} _{-0.15}	12.60 ^{+0.56} _{-0.49}
K20_ID9	2.036	10.92 ^{+0.16} _{-0.11}	7.00 ^{+2.19} _{-1.31}	26.64 ^{+5.03} _{-13.07}	0.46 ^{+0.17} _{-0.17}	12.23 ^{+0.36} _{-0.38}
zC_405501	2.154	10.46 ^{+0.22} _{-0.16}	6.03 ^{+1.34} _{-1.07}	65.68 ^{+4.02} _{-5.99}	0.52 ^{+0.21} _{-0.21}	11.41 ^{+0.44} _{-0.41}
SSA22_MD41	2.172	10.61 ^{+0.24} _{-0.18}	7.98 ^{+1.70} _{-1.27}	72.20 ^{+6.52} _{-6.85}	0.71 ^{+0.15} _{-0.14}	12.05 ^{+0.25} _{-0.24}
BX389	2.180	11.05 ^{+0.27} _{-0.11}	6.81 ^{+1.67} _{-0.87}	80.33 ^{+4.94} _{-8.27}	0.59 ^{+0.14} _{-0.15}	13.06 ^{+0.31} _{-0.34}
zC_407302	2.182	10.66 ^{+0.11} _{-0.10}	5.39 ^{+1.82} _{-1.54}	63.62 ^{+5.29} _{-6.26}	0.61 ^{+0.10} _{-0.09}	12.81 ^{+0.24} _{-0.24}
GS3_24273	2.187	10.91 ^{+0.08} _{-0.08}	8.80 ^{+1.90} _{-1.23}	21.78 ^{+7.65} _{-9.48}	0.25 ^{+0.15} _{-0.10}	11.18 ^{+0.55} _{-0.30}
zC_406690	2.196	11.06 ^{+0.04} _{-0.06}	4.84 ^{+2.26} _{-0.92}	73.39 ^{+7.14} _{-3.11}	0.06 ^{+0.12} _{-0.06}	10.81 ^{+1.46} _{-0.18}
BX610	2.210	11.06 ^{+0.11} _{-0.10}	6.02 ^{+2.02} _{-1.28}	80.39 ^{+5.68} _{-6.41}	0.45 ^{+0.16} _{-0.13}	12.80 ^{+0.45} _{-0.37}
K20_ID7	2.225	10.89 ^{+0.24} _{-0.20}	7.70 ^{+1.40} _{-1.30}	74.30 ^{+4.44} _{-6.97}	0.76 ^{+0.16} _{-0.10}	13.02 ^{+0.22} _{-0.14}
K20_ID6	2.236	10.69 ^{+0.10} _{-0.13}	4.88 ^{+2.61} _{-0.78}	64.70 ^{+7.45} _{-5.33}	0.13 ^{+0.20} _{-0.13}	10.52 ^{+1.23} _{-0.21}
zC_400569	2.242	10.98 ^{+0.09} _{-0.04}	6.18 ^{+2.15} _{-1.51}	71.82 ^{+5.97} _{-8.40}	0.29 ^{+0.12} _{-0.18}	11.92 ^{+0.75} _{-0.73}
BX482	2.258	11.05 ^{+0.23} _{-0.15}	6.58 ^{+0.98} _{-0.79}	71.63 ^{+3.33} _{-4.03}	0.61 ^{+0.17} _{-0.16}	12.93 ^{+0.30} _{-0.27}
COS4_02672	2.308	10.85 ^{+0.22} _{-0.10}	7.08 ^{+1.97} _{-1.24}	64.67 ^{+4.07} _{-4.51}	0.43 ^{+0.20} _{-0.21}	11.61 ^{+0.47} _{-0.42}
D3a_15504	2.383	11.13 ^{+0.12} _{-0.08}	6.40 ^{+1.79} _{-1.30}	69.84 ^{+3.95} _{-4.75}	0.24 ^{+0.13} _{-0.10}	11.68 ^{+0.59} _{-0.41}
D3a_6004	2.387	11.52 ^{+0.07} _{-0.11}	6.05 ^{+2.08} _{-1.08}	68.68 ^{+6.68} _{-6.36}	0.12 ^{+0.17} _{-0.12}	11.93 ^{+1.49} _{-0.26}
GS4_37124	2.431	10.78 ^{+0.15} _{-0.11}	5.17 ^{+1.86} _{-1.23}	68.48 ^{+7.92} _{-13.84}	0.43 ^{+0.11} _{-0.15}	12.33 ^{+0.42} _{-0.54}
GS4_42930	2.451	10.43 ^{+0.15} _{-0.07}	5.17 ^{+1.85} _{-1.31}	56.91 ^{+3.39} _{-4.35}	0.43 ^{+0.16} _{-0.18}	11.35 ^{+0.61} _{-0.61}

^a MCMC MAP values (from the joint posterior distribution) for fits to 1D data, using NFW halos, no adiabatic contraction, and assuming asymmetric drift corrections.^b Calculated from the best-fit $f_{\text{DM}}(R_e)$, $\log_{10}(M_{\text{bar}}/M_{\odot})$, and R_e .

offset $\langle \Delta\sigma_0 \rangle = 8.64 \text{ km s}^{-1}$. Finally, the disk effective radii are overall in very good agreement, though for smaller galaxies the best-fit radii are slightly higher in the MCMC analysis (with an overall median offset of $\langle \Delta R_{e,\text{disk}} \rangle = 0.65 \text{ kpc}$). These median differences are within the typical uncertainties for the two analyses (median uncertainties of $\sim 0.1\text{--}0.14$ for $f_{\text{DM}}(R_e)$, $\sim 0.1\text{--}0.13$ dex for $\log_{10}(M_{\text{bar}}/M_{\odot})$, $\sim 5\text{--}8 \text{ km s}^{-1}$ for σ_0 , and $\sim 1\text{--}2 \text{ kpc}$ for $R_{e,\text{disk}}$).

Generally, these differences in values reflect some of the inherent degeneracies in our models (as discussed in Appendix A.4), modulated by the adopted priors and constraints. For the MCMC analysis, looser constraints on both σ_0 and $R_{e,\text{disk}}$ are adopted, as well a Gaussian prior for $\log_{10}(M_{\text{bar}}/M_{\odot})$. In contrast, the least-squares analysis generally had tight constraints on σ_0 (based on the outermost dispersion points), and adopted top-hat bounds for M_{bar} . In

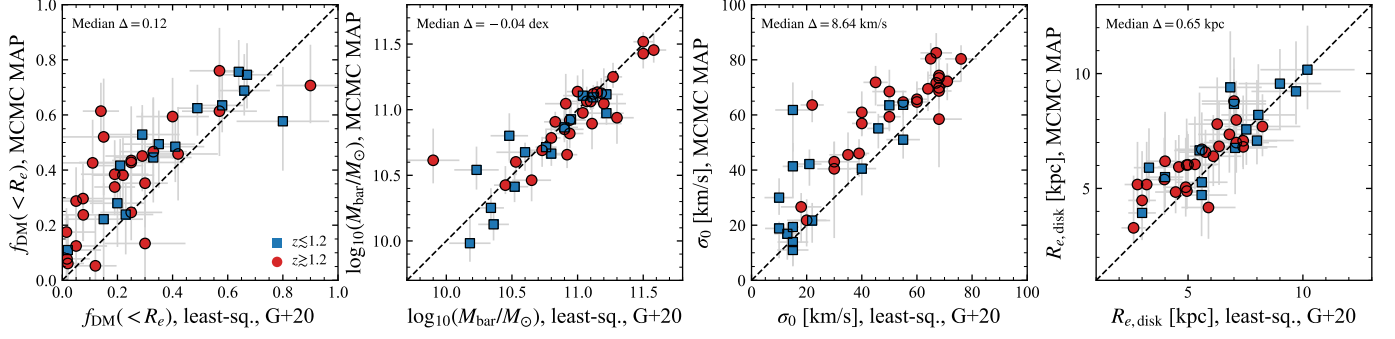


Figure 1. Comparison of the best-fit values of the key dynamical and structural parameters for the RC41 sample from Paper I (least squares) and the 1D MCMC analysis (MAP) presented in this paper. From left to right, we compare $f_{\text{DM}}(R_e)$, $\log_{10}(M_{\text{bar}}/M_{\odot})$, σ_0 , and $R_{e,\text{disk}}$. Galaxies at $z < 1.2$ and $z \geq 1.2$ are marked with blue squares and red circles, respectively. The black dashed line shows the 1:1 relation. The dark matter fractions measured from the MCMC MAP analysis in this paper tend to be higher than those from Paper I by $\Delta f_{\text{DM}}(R_e) \sim 0.1\text{--}0.15$, but the values are consistent within the uncertainties for most galaxies. Paired with the $f_{\text{DM}}(R_e)$ offset, in this paper we tend to find slightly lower baryonic mass values. We tend to find higher intrinsic velocity dispersion values, as the priors adopted in this analysis are *less restrictive* than the bounds in Paper I. The best-fit disk effective radii are fairly similar between the two analyses, though slightly larger in this paper’s analysis.

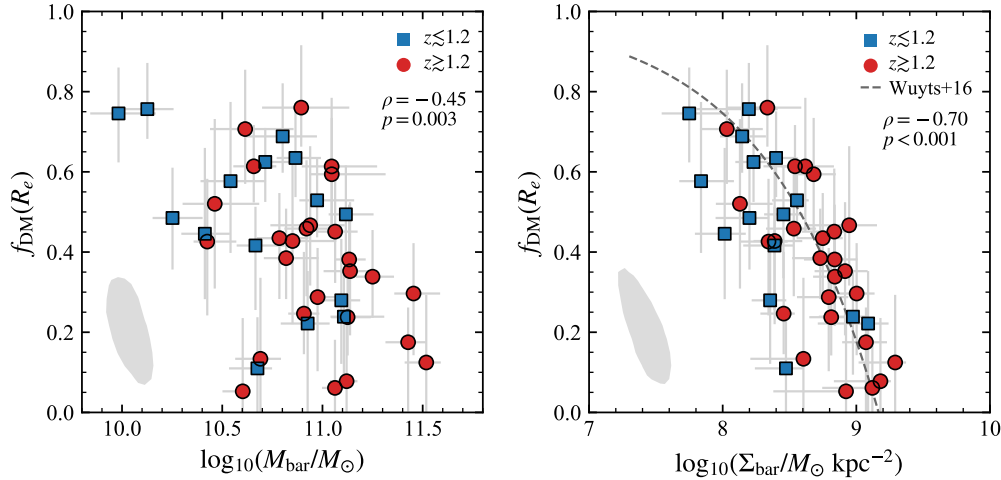


Figure 2. Dark matter fraction versus baryonic mass (left) and versus baryonic surface density (right) using the best-fit results of the 1D MCMC analysis in this paper. The symbol definitions are the same as in Figure 1. The median 1σ uncertainty contours are shown with filled grey regions. The grey dashed line in the right panel shows the relation between Σ_{bar} and $f_{\text{DM}}(R_e)$ from Wuyts et al. (2016). Spearman correlation coefficients and p -values are also shown. We find very similar anti-correlations between $f_{\text{DM}}(R_e)$ and $\log_{10}(M_{\text{bar}}/M_{\odot})$ (moderate, 2.7σ) and between $f_{\text{DM}}(R_e)$ and $\log_{10}(\Sigma_{\text{bar}}/M_{\odot} \text{ kpc}^{-2})$ (strong, 5σ) as reported in Paper I (their Figure 7, lower left and upper right, respectively), though the MCMC MAP $f_{\text{DM}}(R_e)$ values are a bit higher on average, particularly for some of the $z \sim 2$ galaxies.

particular, the looser constraints on σ_0 impacted the MCMC fitting. The increased parameter flexibility resulted in cases where the likelihood is maximized by a higher σ_0 , as the improved match of the model velocity curve to the data outweighed the increased discrepancy with the dispersion profile. In other cases, the overall observed dispersion profile resulted in higher likelihood for models with increased σ_0 . This tendency of higher σ_0 (from the looser σ_0 prior) combines with the effect of the adopted Gaussian priors on $R_{e,\text{disk}}$ and $\log_{10}(M_{\text{bar}}/M_{\odot})$ to impact the best-fit results of our simultaneous 4-parameter MCMC fitting. The higher σ_0 and marginally higher $R_{e,\text{disk}}$ values tend to shift up the DYSMAL model $v_{\text{circ}}(R_e)$ degeneracy ellipse (already moving towards higher $f_{\text{DM}}(R_e)$), and the slightly lower $\log_{10}(M_{\text{bar}}/M_{\odot})$

values translate into higher $f_{\text{DM}}(R_e)$ values (see Figure 7, Appendix A.4).

Despite these small differences in the recovered values between these two approaches, the MCMC analysis confirms that **the majority of galaxies in our sample ($\sim 70\%$), particularly at $z \geq 1.2$, are baryon-dominated on galaxy scales, with $f_{\text{DM}}(R_e) \lesssim 0.5$** . For $\sim 30\%$, the dark matter fractions are similar to or less than that of “maximal disks” ($f_{\text{DM,max}} < 0.28$; Courteau & Dutton 2015). Moreover, the MCMC results recover the same overall trends seen in Paper I, such as the strong anti-correlation of dark matter fraction with baryonic surface density and the moderate (and less significant) anti-correlation of dark matter fraction with total baryonic mass, which we show in Figure 2. **Overall, we find that the least-squares and MCMC results are in good agreement.**

Table 4. Priors for 2D MCMC Fitting^{a,b}

ID	$\log_{10}(M_{\text{bar}}/M_{\odot})$	$f_{\text{DM}}(R_e)$	σ_0	$R_{e,\text{disk}}$	V_{sys}
	[dex]	—	[km s ⁻¹]	[kpc]	[km s ⁻¹]
zC_403741	Gaus(10.86, 0.2); [9, 13]	Flat[0, 1]	Flat[5, 300]	<i>Fixed</i>	Flat[-100, 100]
D3a_6397	Gaus(11.34, 0.2); [9, 13]	Flat[0, 1]	Flat[5, 300]	<i>Fixed</i>	Flat[-130, 70]
zC_405501	Gaus(10.43, 0.2); [9, 13]	Flat[0, 1]	Flat[5, 300]	Gaus(5.0, 2); [1, 15]	Flat[-108, 92]
BX389	Gaus(10.94, 0.2); [9, 13]	Flat[0, 1]	Flat[5, 300]	<i>Fixed</i>	Flat[-180, 20]
zC_407302	Gaus(10.81, 0.2); [9, 13]	Flat[0, 1]	Flat[5, 300]	<i>Fixed</i>	Flat[-150, 50]
zC_406690	Gaus(11.09, 0.2); [9, 13]	Flat[0, 1]	Flat[5, 300]	<i>Fixed</i>	Flat[-75, 125]
BX610	Gaus(11.52, 0.2); [9, 13]	Flat[0, 1]	Flat[5, 300]	Gaus(4.9, 2); [1, 15]	Flat[-100, 100]
K20_ID7	Gaus(10.76, 0.2); [9, 13]	Flat[0, 1]	Flat[5, 300]	<i>Fixed</i>	Flat[-100, 100]
K20_ID6	Gaus(10.80, 0.2); [9, 13]	Flat[0, 1]	Flat[5, 300]	Gaus(5.0, 2); [1, 15]	Flat[-100, 100]
zC_400569	Gaus(11.50, 0.2); [9, 13]	Flat[0, 1]	Flat[5, 300]	<i>Fixed</i>	Flat[-100, 100]
BX482	Gaus(11.00, 0.2); [9, 13]	Flat[0, 1]	Flat[5, 300]	Gaus(5.8, 2); [1, 15]	Flat[-40, 160]
D3a_15504	Gaus(11.28, 0.2); [9, 13]	Flat[0, 1]	Flat[5, 300]	<i>Fixed</i>	Flat[-100, 100]
D3a_6004	Gaus(11.70, 0.2); [9, 13]	Flat[0, 1]	Flat[5, 300]	<i>Fixed</i>	Flat[-100, 100]
GS4_42930	Gaus(10.65, 0.2); [9, 13]	Flat[0, 1]	Flat[5, 300]	<i>Fixed</i>	Flat[-100, 100]

^a Gaussian priors are noted as “Gaus(center, stddev)”, and are additionally bounded within the range [lower, upper]. Flat priors and their boundaries are denoted by “Flat[lower, upper]”.

^b When not fixed, the priors on $\log_{10}(M_{\text{bar}}/M_{\odot})$, $f_{\text{DM}}(R_e)$, σ_0 , and $R_{e,\text{disk}}$ are the same for both the 1D and 2D MCMC fitting.

5. COMPARISON OF DISK FITTING USING 1D AND 2D KINEMATICS

For the RC41 data set, we performed our dynamical analysis using extracted 1D kinematic profiles, to maximize the data S/N and to push to the largest possible radii. For axisymmetric distributions, 2D maps of the galaxy velocity and dispersion fields (or additional higher-order moments) encode additional information about the kinematic position angle and galaxy inclination, and can provide additional constraints on the disk effective radius, $R_{e,\text{disk}}$, or the bulge-to-total ratio, B/T . Given sufficient 2D S/N, it would thus be possible to independently fit for these parameters, instead of adopting values derived from imaging under the assumption that they also apply to the underlying mass distribution, which may be incorrect given intrinsic mass-to-light gradients or optically thick dusty regions in the centers of galaxies. It should be noted, however, that 2D maps can reveal noncircular motions, which capture other physical processes superimposed on the regular disk rotation.

Here we compare 1D and 2D fitting results for a subset of 14 galaxies in the RC41 sample, in order to examine how much dynamical information is captured along the major axis, and to consider the relative benefits of fitting in 1D versus 2D. We then briefly examine non-circular motions seen in the 2D residual maps for one galaxy, and present an example toy model that could describe this additional kinematic signature.

5.1. Disk Modeling: Kinematics Well-Measured by 1D Fitting

In order to maximize the depth of the 2D maps (and therefore pushing to the maximum outer radii), we perform fitting using 2D maps derived from the deepest possible data — generally the composite cubes combining all available AO-assisted and seeing-limited data. The measurement of the 2D maps and the 2D fitting methodology are presented in detail

in Sections 2 and 3.3. The key difference between the 1D and 2D fitting is in the treatment of $R_{e,\text{disk}}$: it is a free parameter for the 1D modeling, but for many cases is poorly constrained by the 2D maps. Thus, for most 2D fits we fix $R_{e,\text{disk}}$ to the best-fit 1D MCMC value. For the 2D fitting we additionally fix the kinematic center and orientation (PA, inclination) for each galaxy, as these parameters can be strongly impacted by asymmetries or non-circular kinematic features (as discussed below).

As an example of the 2D versus 1D fits, in Figure 3 we show the 2D maps, best-fit models, and residuals for three galaxies (second through fourth columns). For comparison with the 1D fits, we also show the best-fit 2D models extracted along the major axis using pseudo-slits versus the observed and best-fit 1D profiles (first column). There is relatively good agreement in the 1D profiles between the data, 1D and 2D best-fit models, though the 1D profiles from the 2D models diverge from the data towards the outskirts in some cases. As discussed below, we attribute these deviations primarily to the impact of non-circular kinematics or asymmetric features on the 2D fits.

When comparing the 1D and 2D fits, we find a relatively good agreement between the two measurements of $f_{\text{DM}}(R_e)$ overall. However, on average the 2D fits tend to find larger dark matter fractions. Furthermore, a good fraction of the galaxies show discrepancies between $f_{\text{DM}}(R_e)_{1\text{D}}$ and $f_{\text{DM}}(R_e)_{2\text{D}}$, up to differences of $|\Delta f_{\text{DM}}(R_e)| \sim 0.45$. For the baryonic masses, there is excellent agreement above $\log_{10}(M_{\text{bar}}/M_{\odot}) \sim 11$, but we tend to find a ~ -0.2 dex offset between the 2D and 1D values for the lower masses (and accordingly generally find higher 2D dark matter fractions). There is scatter between the measured 1D and 2D intrinsic dispersion values, as σ_0 is sensitive to off major-axis features and deviations from pure rotational motion in the 2D maps. Two factors could be responsible for these discrepancies.

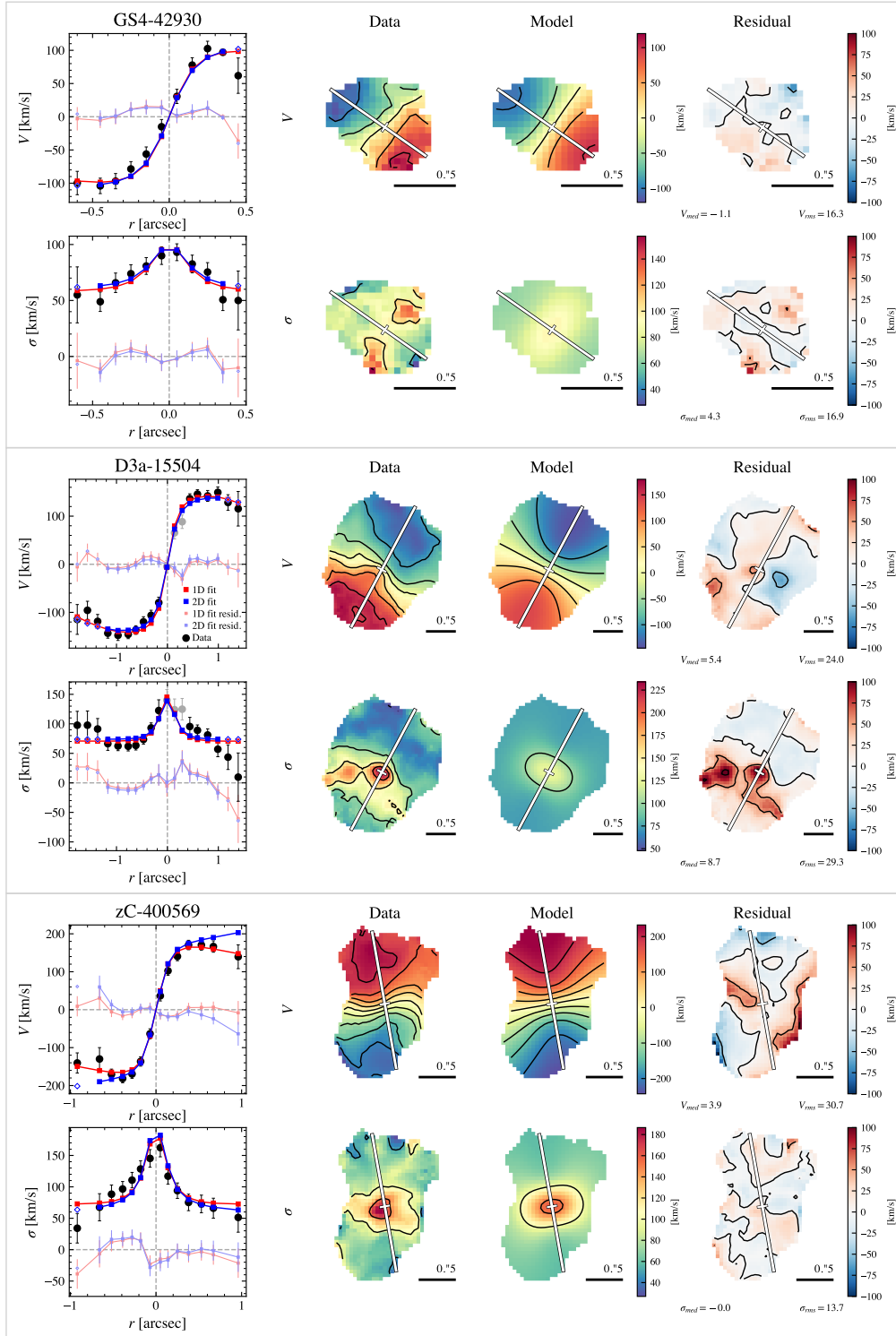


Figure 3. Example 2D fits for 3 galaxies in the RC41 sample. The composite 2D velocity (top) and dispersion (bottom) maps are shown in the second column for each galaxy. The best-fit models and residuals from the 2D fitting are shown in the third and fourth columns. The major axes and centers are marked with white lines on the 2D maps, and contours are marked in 50 km s^{-1} intervals. In the first column, we compare the 1D observed profiles (black circles) with the 1D best-fit models (red squares) and the 2D best-fit models, extracted within the same 1D apertures/PV diagrams (blue points, with filled squares and open diamonds showing $\leq R_{\text{out},2\text{D}}$ and $> R_{\text{out},2\text{D}}$). The 1D residuals for the 1D and 2D models are shown in light red and blue, respectively. Overall, the 1D and 2D fits of the disk kinematics show fairly good agreement, but there are deviations towards larger radii that likely reflect effects from non-circular features. The axisymmetric disk models used in this study work well for galaxies with fairly symmetric kinematics (e.g., GS4-42930). Non-circularities such as PA twists can lead to differences between the 1D and 2D fits (e.g., zC-400569), but in other cases both fits agree despite such features (e.g., D3a-15504). Previously, the 2D disk modeling of D3a-15504 (and other subsample objects) by Cresci et al. 2009 also revealed the primary disk rotation and secondary residual features in this galaxy.

First, there are differences in the 1D and 2D data maximal radial extent (i.e., R_{out} , as noted in Figure 3). The apertures used to extract the 1D profiles help to optimize the data S/N, pushing the kinematic profiles out to large radii, particularly when flared apertures are used. In contrast, the 2D maps are limited by the per-spaxel S/N, and thus are generally limited to smaller galactic radii. For most of the objects in this subset, $R_{\text{out},1\text{D}}$ is greater than $R_{\text{out},2\text{D}}$ by $\sim 0.5\text{--}3$ kpc. The extra radial coverage of the 1D profiles can help to break degeneracies between model parameters, as this better probes regions where dark matter is expected to become more important relative to the baryons. The more extended 1D profiles can also better constrain the intrinsic velocity dispersion, as σ_0 is best probed in regions less impacted by beam smearing (i.e. large galactic radii). We test the relative importance of the data radial extent in our fits by repeating the 1D MCMC fitting using profiles truncated to more closely match $R_{\text{out},2\text{D}}$ (e.g., see left panels of Figure 3). These fits find nearly identical results within the uncertainties to the untruncated 1D fits (with the exception of σ_0 for zC-407302, where the extended 1D profile was crucial to constraining the intrinsic dispersion). Thus, we conclude that while for our subset of 14 galaxies radial extent can play a role in constraining dynamical components, it is not the primary driver of differences between the 1D and 2D fit results.

Second, and more importantly, non-circular kinematics or asymmetric features impact our kinematic fitting, particularly in 2D given the extra off-major axis information. As we fit the data with axisymmetric mass and kinematic models, any asymmetry or non-circular motions can pose problems to the recovery of the intrinsic underlying circular motion of the galaxies. The major axis 1D profiles should be much less sensitive to such issues, as many of these features are not captured along major axis kinematic cuts. We find that most of the objects in our 2D analysis exhibit kinematic asymmetries or non-circular features, which, depending on their nature and strength, can significantly affect results of modeling with axisymmetric-only models. For example, in Figure 3, we show two galaxies exhibiting PA twists in the 2D maps. For one object (zC-400569; bottom), this PA twist is likely responsible for the difference in the 1D and 2D fits, while for the other (D3a-15504; middle) the twist does not strongly impact the 2D fit. In contrast, we would expect more similar 1D and 2D fits for galaxies with fairly symmetric 2D kinematics (e.g., GS4-42930; Figure 3, top). By probing only the major-axis kinematics, the 1D fits may better reflect the underlying disk kinematics and mass distributions than the 2D fits. The non-circular or asymmetric features may drive the 2D fit results away from the intrinsic galaxy properties, complicating a direct comparison between the 1D and 2D values. However, from our current small 2D sample, it is difficult to determine what type and strength of non-circular or asymmetric features impact the 2D disk kinematic fitting.

Based on the general agreement between the 1D and 2D fit $f_{\text{DM}}(R_e)$ values in the modeling framework we consider (i.e., oblate disk, bulge, and halo), we conclude that **the primary**

kinematics of a rotating galaxy are well constrained using 1D fitting along the major axis only. Given the challenges to the 2D kinematic modeling (i.e., data extent; purely axisymmetric models), the underlying disk kinematics may be better constrained by fitting in 1D than in 2D.

5.2. Other Kinematic Signatures in 2D Maps

While 1D major axis profiles capture the key rotational kinematics of disk galaxies, 2D (or 3D) kinematic data are needed to probe higher-order dynamical effects caused by, e.g., perturbations, radial inflows, or outflows. Most of the galaxies in our 2D subsample exhibit signatures of noncircular motions, highlighted in previous work (for example, Genzel et al. 2006, 2008, 2011, 2017, 2020, Förster Schreiber et al. 2009, 2018, Cresci et al. 2009). These features include, notably, twists in the kinematic major axis, other residual features along the minor axis, perturbations likely stemming from interactions with a neighbor/lower-mass satellite, and features resulting from nuclear outflows due to AGN or stellar feedback from bright off-center clumps. Some objects show signs of multiple types of features.

To illustrate the secondary signatures from noncircular motions seen in the 2D kinematics, we examine the case of D3a-15504, for which the kinematics show some of the most suggestive features of radial inflow (Genzel et al. 2006). We construct a toy model combining disk rotation with radial inflow as follows. We first subtract the best-fit galaxy+halo model (determined from the 1D MCMC fits) from the 2D AO kinematic maps, yielding initial velocity and dispersion residual maps. For this galaxy, the velocity residual (Figure 4, top left) shows a central residual bimodality, and a larger-scale bimodal “twist”. The dispersion residual shows a large central excess, which primarily reflects the nuclear outflow seen in this galaxy (Genzel et al. 2006, Förster Schreiber et al. 2014). We then construct a second model (shown in Figure 4, third column), superimposing a constant radial inflow component on top of the best-fit 1D MCMC galaxy+halo model. The radial inflow velocity v_r is manually adjusted (explored with a grid search). We find that a constant radial inflow component of $v_r \sim 90 \text{ km s}^{-1}$ can explain much of the original kinematic residuals (see Figure 4, last column), removing much of the large-scale “S” twist from NE to SW and the central velocity bimodality seen in the galaxy+halo-only velocity residual map. The remaining minor-axis velocity bimodality and central dispersion peak are likely due to the AGN-driven outflow in this galaxy (as noted in Genzel et al. 2006), but we do not attempt to model the outflow for this toy model. While including an inflow component is not necessary to improve the 2D disk fit properties for D3a-15504 (as the 1D and 2D fits agreed well, see Figure 3), for other objects the inclusion of secondary kinematic components could lead to refined 2D disk fits that are in better agreement with the 1D major axis fits.

This initial exploration highlights how deep 2D kinematic maps, particularly from high-resolution adaptive optics-assisted observations, can constrain other dynamical signa-

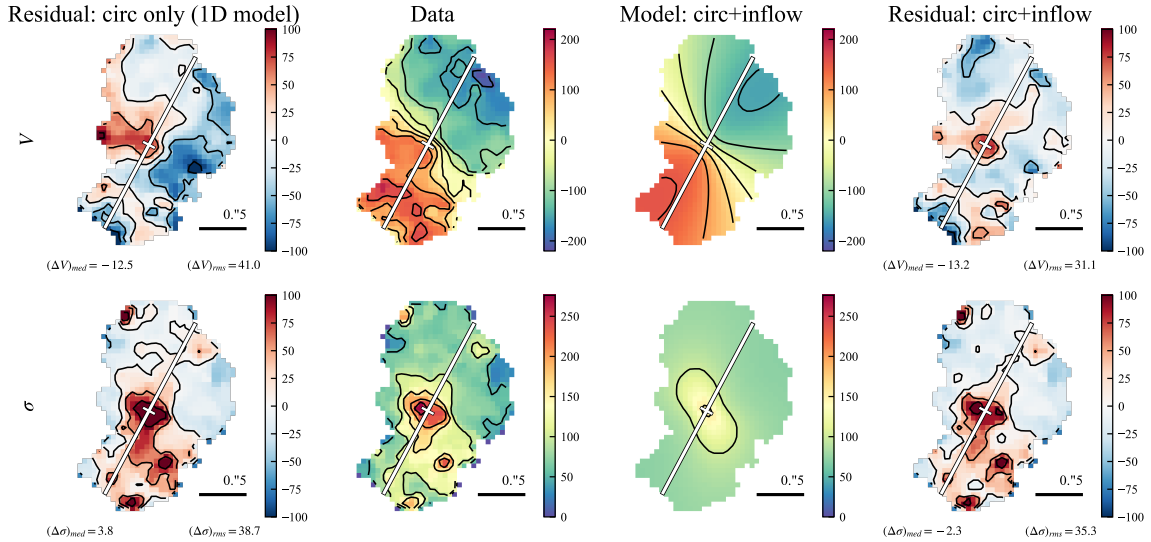


Figure 4. Velocity (top) and dispersion (bottom) maps (with scales in units of km s^{-1}) of one object, D3a-15504, from the 2D fitting subset that exhibits non-circular motions. Here we use maps derived using only the AO data, to maximize the spatial resolution in the central regions of the galaxy. The maps have been median smoothed with a kernel of 3×3 pixels, and we show contours every 50 km s^{-1} . The first column shows the residual maps for the galaxy+halo model determined with 1D MCMC fitting, with appropriate x_0, y_0, V_{sys} applied. The observed AO maps are shown in the second column. We then show an example 2D model in the third column, where we use the same disk+bulge and halo parameters from the 1D fit but manually add a constant radial inflow velocity of $v_r \sim 90 \text{ km s}^{-1}$ (determined by eye after a grid search). The residuals from this composite rotation and radial motion model are shown in the last column. While this is *not* a fit to the data, this example rotation+inflow model reduces the bimodal velocity residual at the center of the galaxy that is perpendicular to the major axis. The test composite model also largely captures the large-scale “S” twist in the rotation velocity. The AGN-driven outflow in this galaxy likely explains the remaining minor-axis velocity bimodality and central dispersion peak.

tures beyond just disk rotation. An extended analysis of the non-circular kinematic signatures in this sample (and in further observations) will be explored in greater detail in future work.

6. DISCUSSION

6.1. Multiple Studies and Approaches Find Consensus: Massive SFGs at $z \sim 1-2$ are Baryon-Dominated

In the previous sections, we have shown that multiple fitting approaches produce similar results for our sample of 41 massive, extended galaxies at $z \sim 1-2$. Whether performing least-squares fitting (as in Paper I) or MCMC sampling of 1D rotation curves extracted along the major axis, or if using the more detailed 2D rotation and dispersion maps, the best-fit values of $f_{\text{DM}}(R_e)$, $\log_{10}(M_{\text{bar}}/M_{\odot})$, σ_0 , and $R_{e,\text{disk}}$ are all in relatively good agreement. These results are also consistent with those of Genzel et al. (2017) and Übler et al. (2018), which together analyzed seven galaxies that are included in the RC41 sample.

One key result from our analyses of the RC41 sample is that there is a strong anti-correlation between $f_{\text{DM}}(R_e)$ and the baryonic surface density (Figure 8 of Paper I; also Figure 2). However, we selected large galaxies to maximize the number of spatial resolution elements, and thus our sample does not include many small, high-density galaxies. We thus compare the RC41 results to the findings of “inner dynamics” analyses, which use kinematic signatures on less-extended scales (i.e., $\lesssim R_e$) in combination with separate measurements of M_{bar} or M_* to estimate the baryonic and dark matter frac-

tions. Kinematic measurements on these scales can be performed for larger samples extending to smaller galaxy sizes than when fitting to outer rotation curves, as the depth and resolution requirements are lower.

There is good agreement between observations from such “inner dynamics” studies of individual massive star-forming galaxies and our RC41 analysis. Wuyts et al. (2016) find a very similar trend between $f_{\text{DM}}(R_e)$ and $\log_{10}(\Sigma_{\text{bar}}/M_{\odot} \text{ kpc}^{-2})$ for a sample of 240 galaxies (as discussed in Paper I), and other studies find high baryon fractions towards smaller sizes and higher densities, and with increasing redshift (e.g., van Dokkum et al. 2015, Price et al. 2016, 2020). These results are also consistent with the simulation work of galaxies at this epoch. In particular, Lovell et al. (2018) find a similar anti-correlation of $f_{\text{DM}}(R_e)$ and baryonic surface density (as shown in Paper I; M. R. Lovell 2020, private communication), and Zolotov et al. (2015) find that galaxies are baryon-dominated during times when they are very compact. The general trend of decreasing $f_{\text{DM}}(R_e)$ towards higher redshifts is further supported by the stellar and baryonic Tully-Fisher zero-point evolution found by Übler et al. (2017) and the numerical simulations presented by Teklu et al. (2018).

The literature studies discussed above all constrain the enclosed f_{DM} on galaxy scales (i.e., $r = R_e$ or $R_{e,\text{disk}}$) using the observed kinematics of individual galaxies. Other studies stack the rotation profiles of many galaxies to probe out to even larger galactic radii. Lang et al. (2017) stacked the RCs of rotating disk galaxies at $z \sim 0.6-2.6$, with the indi-

vidual curves normalized at the peak v_{rot} and corresponding radius, and found an average dropping outer RC. By comparing the stack to models consisting of thick exponential disks with σ_0 typical of the stacked sample embedded in a NFW halo, Lang et al. (2017) found that high baryonic fractions on galactic scales are required to match the stacked RC, in excellent agreement with the findings of Paper I and this analysis. A different approach was adopted by Tiley et al. (2019), who instead stacked RCs normalized at $3R_d \sim 1.8R_e$ based purely on the stellar light distribution. Tiley et al. (2019) then compared their stacked RCs to models combining an infinitely thin exponential disk and a pseudo-isothermal dark matter halo, and found the stacks are consistent with low average baryonic fractions within $6R_d \sim 3.6R_e$ (i.e., high average f_{DM}). However, it is difficult to compare the results between these studies because of the different methodologies, and importantly, the sample selections differ and thus differently represent the underlying population. We stress also the importance of the radius within which the enclosed f_{DM} is referenced, as it obviously will increase towards outer regions. As highlighted by Übler et al. (2018), and from examination of the results for the RC41 sample, large or even dominant enclosed f_{DM} around $\sim 3.6R_e$ is not in contradiction with strongly sub-dominant f_{DM} at $\lesssim 1R_e$. More importantly, the enclosed $f_{\text{DM}}(r)$ may provide clues as to the relative concentration of baryons and dark matter as galaxies build up over time, as discussed in Paper I.

After accounting for analysis differences, these other studies are in remarkable agreement with the results of our RC41 work. This reinforces the growing consensus that massive star-forming galaxies at $z \sim 1-2$ tend to be baryon-rich on galaxy scales (i.e., $\sim 1R_e$), with decreasing dark matter fractions as galaxies become more compact. Furthermore, these findings suggest that galaxies with low dark matter fractions have cored halos, as the virial masses inferred from the measured $f_{\text{DM}}(R_e)$ for a NFW profile fall far short of the predictions from stellar mass-halo mass relations (as shown in Figs. 9 & 10 of Paper I). Theoretical studies, though primarily targeting dwarf galaxies or galaxy clusters, show that dark matter core formation can occur due to dynamical friction from infalling clumps (e.g., El-Zant et al. 2001, Mo & Mao 2004, Johansson et al. 2009, Romano-Díaz et al. 2009, Goerdt et al. 2010, Cole et al. 2011, Nipoti & Binney 2015), bars (e.g., Weinberg & Katz 2007), vigorous, fluctuating outflows (e.g., Dekel & Silk 1986, Navarro et al. 1996, Read & Gilmore 2005, Mashchenko et al. 2008, Pontzen & Governato 2012, 2014, Martizzi et al. 2013, Freundlich et al. 2020, K. Dolag et al., in prep.), or impulsive heating from minor mergers (Orkney et al. 2021). Similar physical processes could potentially lead to cored dark matter halos in the massive, gas-rich, star-forming galaxies at $z \sim 1-2$.

6.2. On the role of high velocity dispersion at high redshifts

A complication of the measurement of dark matter fractions is the degeneracy between baryonic disk and dark matter halo. In local galaxies, the relatively high halo concen-

tration contributes to the “disk-halo” conspiracy, where it is difficult to detangle the velocity profiles of the disk and halo on the galaxy scale, making it hard to distinguish between their mass contributions. At higher redshifts, lower concentrations of halos at fixed stellar mass should help to break this degeneracy, by moving the halo profile signatures to larger radii (as discussed in Paper I).

For galaxies with relatively high intrinsic velocity dispersion (e.g., $\sigma_0 \gtrsim 50-60 \text{ km s}^{-1}$), the exponential disk asymmetric drift correction (from Burkert et al. 2010) predicts a marked reduction of the rotation velocity at $\gtrsim R_{e,\text{disk}}$ and a truncation of the disk by roughly a few times the effective radius. Under the right conditions, and together with the impact of beam-smearing, this can result in very similar rotation curves for models with both low and high dark matter fractions. This added degeneracy complication highlights the importance of simultaneously fitting both the rotation and velocity dispersion profiles, to obtain the best possible constraints on the dynamical parameters.

We highlight an extreme example of the added complication of asymmetric drift to the disk-halo degeneracy in Figure 5: zC-405501. This galaxy has a very broad likelihood degeneracy between $f_{\text{DM}}(R_e) - \log_{10}(M_{\text{bar}}/M_{\odot})$ that is strongly impacted by the asymmetric drift correction. In the left panel, we show a low dark matter fraction model, with $f_{\text{DM}}(R_e) = 0.01$, $\log_{10}(M_{\text{bar}}/M_{\odot}) = 10.74$, and $\sigma_0 = 60 \text{ km s}^{-1}$, while the right panel shows a moderately high dark matter fraction model of $f_{\text{DM}}(R_e) = 0.52$, $\log_{10}(M_{\text{bar}}/M_{\odot}) = 10.46$, and $\sigma_0 = 65 \text{ km s}^{-1}$. All other parameters are the same between both models (i.e., $B/T = 0.07$, $R_{e,\text{disk}} = 6 \text{ kpc}$, $n_{S,\text{disk}} = 0.2$). We show the intrinsic baryon, dark matter, and total circular velocity curves for both cases (with the green, purple, and blue solid curves, respectively), and also mark σ_0 (orange dashed line) and the dark matter fraction as a function of radius (grey solid line). The rotation velocity profile determined by applying the asymmetric drift correction to the total circular velocity is shown as the solid black line. The disparity of dark matter fractions is clearly seen in the halo velocity curves, but both models have a fairly similar total circular velocity at $R_{e,\text{disk}}$ (dotted grey line). Furthermore, the asymmetric drift correction produces v_{rot} curves with similar shapes outside of the smallest radii, including similar truncation radii. We note that the slightly higher intrinsic dispersion of the high $f_{\text{DM}}(R_e)$ case ($\sigma_0 = 65 \text{ km s}^{-1}$ versus 60 km s^{-1}) is responsible for matching the truncation radius of the lower $f_{\text{DM}}(R_e)$ case (as the truncation radius would be higher if σ_0 were the same).

When including all observational effects in the models for this extreme case (inclination, beam smearing, and extraction in flared rectangular apertures; red open squares), both low and high dark matter fraction models describe the observed data (grey-outlined circles) fairly well. In particular, the intrinsic small radii differences have been washed out by beam smearing, and both cases follow the dropping profile of the observed velocity curve, thanks to the strong effects of the asymmetric drift correction. If σ_0 is very well constrained

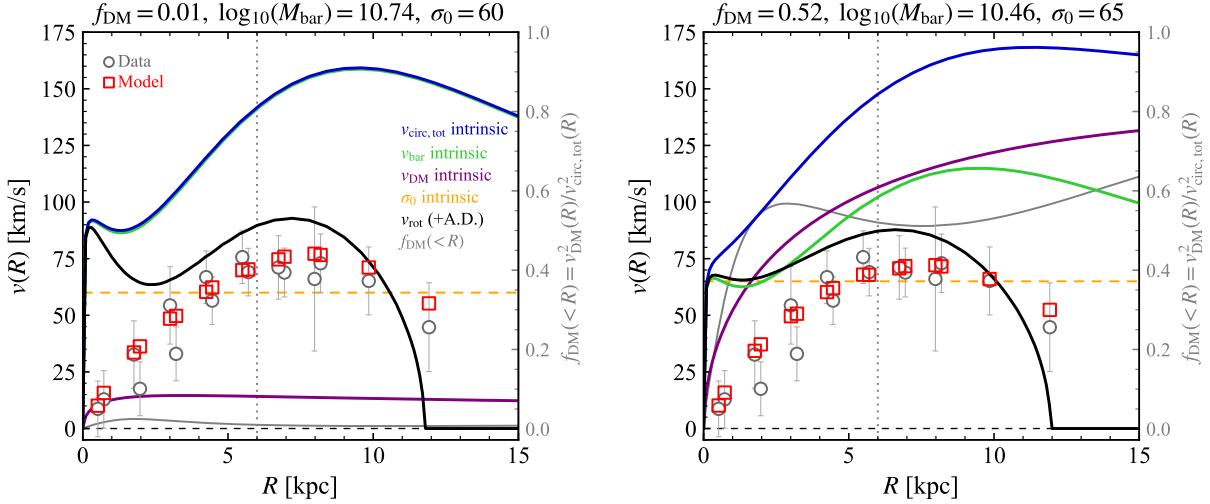


Figure 5. Two example galaxy + halo models in an extreme case demonstrating the degeneracy of models with negligible ($f_{\text{DM}}(R_e) = 0.01$, left) and relatively high ($f_{\text{DM}}(R_e) = 0.52$, right) dark matter fractions because of the strong effects of asymmetric drift at relatively high intrinsic velocity dispersions ($\sigma_0 \sim 60-65 \text{ km s}^{-1}$). The intrinsic baryonic, dark matter, and total circular velocity profiles are shown as green, purple, and blue solid lines, respectively, and the intrinsic velocity dispersion is marked with the dashed orange line. The intrinsic rotation velocity profile, including the effects of asymmetric drift (using Eq. A4, as in Burkert et al. 2010), is shown as the solid black line. The solid grey line shows the dark matter fraction. $R_{e,\text{disk}}$ is marked with the dotted vertical line. The folded 1D observed velocity profile for zC-405501 is shown with the grey-outline points. We also extract the models from the fully forward-modeled cubes using the same apertures (red open squares). The respective $f_{\text{DM}}(R_e)$ and $\log_{10}(M_{\text{bar}}/M_{\odot})$ of the models result in similar values of $v_{\text{circ}}(R_e)$, while the slight σ_0 variation controls the disk truncation radius. Thus, depending on how large σ_0 is and how well it is constrained, it is possible for asymmetric drift to contribute to the degeneracy between disk and halo, even at this early epoch ($z \sim 1-2$) with less concentrated halos when the disk-halo conspiracy should be less problematic.

from the dispersion profile, the added impact of asymmetric drift can be partially mitigated, but for the case of zC-405501, the uncertainties on $\sigma(r)$ (typically $\sim 10-15 \text{ km s}^{-1}$) allow room for a slightly higher σ_0 to better match the falloff for the 52% dark matter fraction case. Observations with higher spatial resolution can also help to break this added degeneracy, as the intrinsic rotation curves (solid black lines) exhibit shape differences at small radii.

Nonetheless, the similarity of the 1D “observed” model profiles in these two cases highlights how it is still possible to have strong disk-halo degeneracies, even at these redshifts, as in the high-dispersion limit (with some uncertainty) the asymmetric drift correction can produce strong turnovers even in dark-matter dominated models. We note that the pressure support corrections used here are based on simple assumptions (i.e., a self-gravitating disk). Further constraints will help to determine the most applicable pressure correction for galaxies at these redshifts.

7. SUMMARY

In this paper, we present a companion analysis of the kinematics for a sample of 41 large, massive, star-forming galaxies at $z \sim 1-2$, which were first published in Genzel et al. (2020) (Paper I). As in Paper I, we fit the 1D rotation curves using fully forward-modeled 3D kinematic models extracted to match the observations, but for this analysis we use MCMC sampling to derive maximum a posteriori (MAP) “best-fit” values and to estimate the fit uncertainties. We additionally fit the kinematics for a subset of 14 galaxies using the spatially-

resolved 2D rotation and dispersion maps. Our key findings are as follows:

- (i) **Multiple approaches reinforce the finding that massive SFGs at $z \sim 1-2$ are baryon-dominated on galactic scales.** We find good agreement between the measured kinematic and mass parameters for the 1D least-squares analysis of Paper I and the 1D MCMC analysis presented here. Additionally, there is relatively good agreement between the $f_{\text{DM}}(R_e)$ values measured from the 1D and 2D MCMC fitting analysis for the subset of galaxies considered. The agreement between these three fitting methodologies, and with the results from other work (e.g., van Dokkum et al. 2015, Wuyts et al. 2016, Price et al. 2016, 2020), demonstrates the robustness of our findings that massive galaxies at these redshifts are generally baryon-dominated, with low galaxy-scale ($\sim 1R_e$) dark matter fractions.
- (ii) **Primary disk kinematics are well captured along the major axis.** The agreement of the 1D and 2D kinematic fitting further supports that most of the kinematic information about disk dynamics and intrinsic dispersion for these high-redshift galaxies is encoded along the major axis.
- (iii) **Evidence for noncircular motions.** The data show evidence for noncircular motions, in addition to the disk kinematics for many of the galaxies in our 2D analysis subset. These features can affect the results of modeling in 2D. We show that a toy model with constant radial in-

flow can explain some of the noncircular residuals for one of these objects (D3a-15504).

Future work will expand on the analysis presented here and in [Paper I](#). Efforts are ongoing to construct even larger samples of high-quality individual rotation curves, that will provide further insights into population and evolutionary trends in the dynamical structures and dark matter fractions of galaxies at $z \sim 0.5-2$. Additionally, future observations of molecular gas with NOEMA and ALMA, and of ionized gas with VLT/ERIS and *JWST*, will allow us to push these detailed dynamical studies to populations at $z \gtrsim 3$. Finally, we will examine the non-circular motions of $z \sim 1-2$ galaxies in detail, using existing and future high-resolution data. These high-resolution data will allow us to consider not only the general mass distributions in these galaxies, but to also constrain the internal dynamical processes that play key roles in the build-up and evolution of galaxies – in particular, the build-up of bulges, which is expected to be rapid at this epoch, and that may be accompanied by the “coring” of the galaxies’ dark matter halos.

ACKNOWLEDGMENTS

We thank our colleagues at MPE, ESO-Garching and ESO-Paranal, LBT and IRAM, and members of the 3D-HST, SINFONI/SINS & zC-SINF and KMOS/KMOS^{3D} teams, who have contributed to, helped, or otherwise supported these observations and their analysis. We also thank the anonymous referee for their valuable feedback and suggestions that improved this manuscript. The data analyzed here are based on H α observations collected with the integral field spectrometers SINFONI (SINS & zC-SINF surveys, plus open time programs) and KMOS (KMOS^{3D} guaranteed time survey) obtained at the Very Large Telescope (VLT) of the European Southern Observatory (ESO), Paranal, Chile (under ESO programmes 073.B-9018, 074.A-9011, 075.A-0466, 076.A-0527, 077.A-0527, 078.A-0600, 079.A-0341, 080.A-0330, 080.A-0339, 080.A-0635, 081.A-0672, 081.B-0568, 082.A-0396, 183.A-0781, 087.A-0081, 088.A-0202, 088.A-0209, 090.A-0516, 091.A-0126, 092.A-0082, 092.A-0091, 093.A-

0079, 093.A-0110, 093.A-0233, 094.A-0217, 094.A-0568, 095.A-0047, 096.A-0025, 097.A-0028, 098.A-0045, 099.A-0013, 1000.A-0039, 1000.A-0361, and 10102.B-0087). The analysis also includes CO observations within the PHIBSS1 and PHIBSS2 open time large projects, and the NOEMA^{3D} guaranteed time project, at the Northern Extended Array for Millimeter Astronomy (NOEMA, located on the Plateau de Bure) Interferometer of the Institute for Radio Astronomy in the Millimeter Range (IRAM), Grenoble, France. IRAM is supported by INSU/CNRS (France), MPG (Germany), and IGN (Spain). Finally, this work includes H α slit spectroscopy obtained with the LUCI spectrometer at the Large Binocular Telescope (LBT) on Mount Graham, Arizona, USA. The LBT is an international collaboration among institutions in the United States, Italy, and Germany. LBT Corporation partners are: LBT Beteiligungsgesellschaft, Germany, representing the Max-Planck Society, The Leibniz Institute for Astrophysics Potsdam, and Heidelberg University; The University of Arizona on behalf of the Arizona Board of Regents; Istituto Nazionale di Astrofisica, Italy; The Ohio State University, and The Research Corporation, on behalf of The University of Notre Dame, University of Minnesota and University of Virginia. This work was supported in part by the Deutsche Forschungsgemeinschaft (DFG, German Research Foundation) within the Deutsch-Israelische Projektkooperation (DIP, German-Israeli Project Cooperation) under DFG/DIP grant STE/1869 2-1 / GE 625/17-1. TN acknowledges support by the Excellence Cluster ORIGINS which is funded by the DFG under Germany’s Excellence Strategy – EXC-2094 – 390783311.

Software: Astropy⁴ (Astropy Collaboration et al. 2013, 2018), emcee (Foreman-Mackey et al. 2013), corner (Foreman-Mackey 2016), IPython (Pérez & Granger 2007), Matplotlib (Hunter 2007), MPFIT (Markwardt 2009), Numpy (Van Der Walt et al. 2011; Harris et al. 2020), Pandas (McKinney 2010; The pandas development team 2020), Photutils (Bradley et al. 2019, 2020), Scipy (Virtanen et al. 2020)

Facilities: VLT:Antu (KMOS), VLT:Yepun (SINFONI), IRAM:NOEMA, LBT (LUCI)

APPENDIX

A. `DysmalPy`: DYNAMICAL DISK MODELING WITH DYSMAL

DYSMAL is a code that uses a set of physical model mass and kinematic components to describe and fit the kinematics of galaxies. Here, we discuss `DysmalPy`, which implements and extends the DYSMAL fitting models that were introduced in Cresci et al. (2009) and Davies et al. (2011), and includes subsequent improvements described in Wuyts et al. (2016), Genzel et al. (2017), and Übler et al. (2018). Specifically,

this new implementation in `python` now includes multiple halo models, outflow components, the ability to tie model component parameters together, and the choice of fitting using either least-squares minimization or Markov Chain Monte Carlo (MCMC) posterior sampling.

In this Appendix, we describe how a DYSMAL model is used to forward-model a full 3D mock cube $I_{\text{mod}}(x_{\text{sky}}, y_{\text{sky}}, V_{\text{los}})$ that captures the composite kinematics, and accounts for all observational effects (including beam smearing and instrumental line broadening). This model cube can be either retained for 3D cube comparisons, or can

⁴ <http://www.astropy.org>

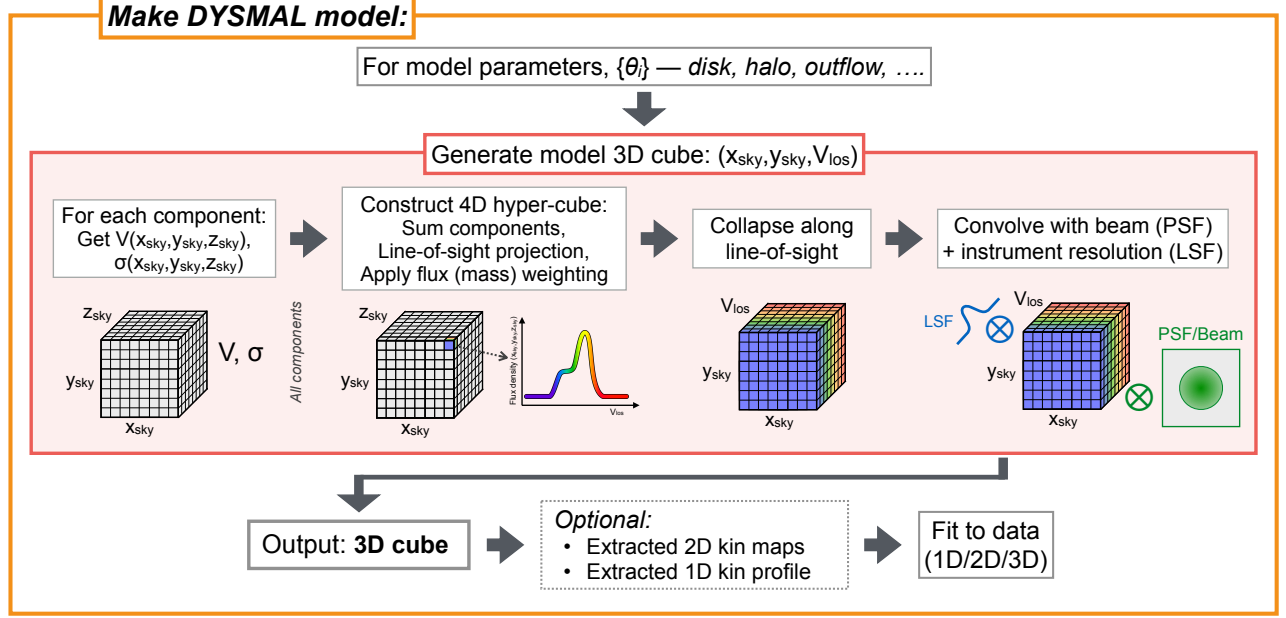


Figure 6. Schematic of how `DysmalPy` models are generated. The process involves a full forward modeling of the components in the sky frame (x, y, z) , construction of a composite 4D hyper-cube including line-of-sight projection and flux weighting, a collapse along the line-of-sight to determine $I_{\text{intr.}}(x, y, V)$, and convolution with the instrument beam and response (i.e., PSF and LSF) to yield a 3D cube. This 3D model cube can then be directly compared to data cubes, or can be further processed for comparison to 1D kinematic profiles or 2D kinematic maps.

be directly compared to 2D or 1D kinematic observations by extracting 2D maps or 1D profiles following the same procedure that was applied to the observed data. We then describe the procedures for fitting the DYSMAL model to observed data, either using MCMC or least-squares fitting.

As the DYSMAL model creation fully forward-models the galaxy kinematics, it is possible to directly fit for the intrinsic galaxy properties. Furthermore, because DYSMAL relies directly on mass distribution and kinematic profile parameterizations, these models allow for direct exploration of mass decomposition and dark matter fractions in galaxies, as well as any degeneracies or uncertainties in these physical quantities, as opposed to non-parametric kinematic fitting that requires further steps to interpret the recovered intrinsic galaxy kinematics.⁵

A.1. Definition of DYSMAL Kinematic Models

At their core, DYSMAL models are a composite set of mass and kinematic components, together with other galaxy properties, which together describe the mass profile, light profile, other kinematic components, and geometry of a galaxy. These components, along with galaxy and instrument parameterizations, are used to compute a full composite mock 3D cube $I_{\text{mod}}(x_{\text{sky}}, y_{\text{sky}}, V_{\text{los}})$ that is comparable to real observed integral field spectrograph cubes. The procedure for producing a mock 3D cube from the galaxy components and

parameterizations is as follows. We also outline the major steps in the process in Figure 6, and in Table 5 present an overview of the possible model components that can be used with `DysmalPy`.

We begin by defining an intrinsic coordinate system $(x_{\text{gal}}, y_{\text{gal}}, z_{\text{gal}})$ for the galactic system. We define $x_{\text{gal}}, y_{\text{gal}}$ as the position within the galaxy midplane (so $R_{\text{gal}} = \sqrt{x_{\text{gal}}^2 + y_{\text{gal}}^2}$ is the radial distance from the rotational axis), and z_{gal} to be the vertical position (which is parallel to the rotational axis). The y_{gal} axis is taken to be the axis about which the galaxy is inclined on the sky (so the projected major axis coincides with the y_{gal} axis).

The galactic system is then inclined at an angle i relative to the line of sight (with $i = 0^\circ, 90^\circ$ corresponding to face-on and edge-on orientations, respectively), and the major axis (blue side; \hat{y}_{gal}) is oriented at an angle PA counter-clockwise from the upward direction in the observations (e.g., often angle East of North). The transformation from the sky coordinates back to the intrinsic galaxy coordinates is then

$$\begin{aligned}
 x_{\text{gal}} &= \left[(x_{\text{sky}} - x_0) \cos \text{PA} - (y_{\text{sky}} - y_0) \sin \text{PA} \right] \cos i \\
 &\quad - z_{\text{sky}} \sin i \\
 y_{\text{gal}} &= (x_{\text{sky}} - x_0) \sin \text{PA} + (y_{\text{sky}} - y_0) \cos \text{PA} \\
 z_{\text{gal}} &= \left[(x_{\text{sky}} - x_0) \cos \text{PA} - (y_{\text{sky}} - y_0) \sin \text{PA} \right] \sin i \\
 &\quad + z_{\text{sky}} \cos i,
 \end{aligned} \tag{A1}$$

where (x_0, y_0) is the center of the galaxy within the observation field of view.

⁵ Other approaches to kinematic fitting that use forward modeling to directly account for observational effects include GalPaK^{3D} (another parametric approach; Bouché et al. 2015) and ^{3D}BAROLO (non-parametric, tilted ring modeling; Di Teodoro & Fraternali 2015).

Table 5. Possible Model Components in `DYSMALPy`

Components	Key Parameters
Black hole	M_{BH}
Freeman disk	Σ_0, r_d
Sérsic (flattened or spherical) <i>e.g.: Disk + bulge</i>	n_S, q_0, R_e $n_{S,\text{disk}}, q_{0,\text{disk}}, R_{e,\text{disk}};$ $n_{S,\text{bulge}}, q_{0,\text{bulge}}, R_{e,\text{bulge}}$
Dark matter halo	
<i>NFW</i>	$\log_{10}(M_{\text{vir}}/M_\odot)$ or $f_{\text{DM}}(R_e), c_{\text{halo}}$
<i>Two-power halo</i>	$\alpha_{\text{inner}}, \beta, \log_{10}(M_{\text{vir}}/M_\odot), c_{\text{halo}}$
<i>Burkert</i>	$r_B, \log_{10}(M_{\text{vir}}/M_\odot)$
<i>Einasto</i>	$\alpha_{\text{Ein}}, \log_{10}(M_{\text{vir}}/M_\odot), c_{\text{halo}}$
<i>Dekel-Zhao</i>	$\log_{10}(M_{\text{vir}}/M_\odot), s_1, c_2$
Intrinsic velocity dispersion	
<i>Isotropic</i>	σ_0
Biconical Outflow	$\theta_{\text{inner}}, \theta_{\text{outer}}, i_{\text{out}}, r_{\text{end}}, n, \tau, A, v_{\text{max}}$
Radial motion / flow	
<i>Constant radial flow</i>	v_r

Next, for each mass component in the model, the mass distribution is used to determine the circular velocity within the midplane, $v_{\text{circ,comp}}(R_{\text{gal}}, z_{\text{gal}} = 0)$. If the component is flattened, the modified circular velocity curve is included here. The composite circular velocity curve is then found by summing in quadrature:

$$v_{\text{circ,tot}}^2(R_{\text{gal}}) = \sum_{\text{comp } i} v_{\text{circ},i}^2(R_{\text{gal}}). \quad (\text{A2})$$

Alternatively, if adiabatic contraction of the halo component is to be included, the total circular velocity is instead calculated using the implicit equation from Burkert et al. (2010) (Eqs. 18 & 19):

$$v_{\text{circ,tot}}^2(R_{\text{gal}}) = v_{\text{bary,tot}}^2(R_{\text{gal}}) + v_{\text{halo}}^2(R'), \quad (\text{A3})$$

$$R' = R_{\text{gal}} \left[1 + \frac{R_{\text{gal}} \times v_{\text{bary,tot}}^2(R_{\text{gal}})}{R' \times v_{\text{halo}}^2(R')} \right],$$

$$\text{with } v_{\text{bary,tot}}^2(R_{\text{gal}}) = \sum_{\text{baryonic comp } i} \left[v_{\text{circ},i}^2(R_{\text{gal}}) \right].$$

For simplicity, we assume this total $v_{\text{circ,tot}}(R_{\text{gal}})$ is independent of z_{gal} , or $v_{\text{circ,tot}}(R_{\text{gal}}, z_{\text{gal}}) = v_{\text{circ,tot}}(R_{\text{gal}}, 0)$ (i.e. cylindrical shells of constant circular velocity).

Mass components that are implemented in `DYSMAL` include Sérsic components with or without flattening (following Noordermeer 2008), which can be used to describe disk (e.g., flattened and $n_S \sim 1$) and bulge (e.g., spherical or flattened and $n_S \sim 4$) baryonic components. Tables with pre-computed rotation curves following Noordermeer (2008) have been calculated for $n_S = 0.5, \dots, 8$ in steps of 0.1, with inverse $1/q_0 = [1, 2, 3, 4, 5, 6, 8, 10, 20, 100]$. The pre-computed rotation curves with the nearest n_S and q_0 are then used when including a deprojected (flattened or spherical) Sérsic mass component (i.e., when $n_{S,\text{disk}} < 0.5$, $n_S = 0.5$ rotation curves are used, but $n_{S,\text{disk}}$ is used for the light distribution; see below). Also included are halos following NFW

(Navarro et al. 1996), Two-Power (Binney & Tremaine 2008), Burkert (Burkert 1995), Einasto (Einasto 1965), and Dekel-Zhao (Dekel et al. 2017, Freundlich et al. 2020) profiles.

The intrinsic dispersion profile of the model, $\sigma(x_{\text{gal}}, y_{\text{gal}}, z_{\text{gal}})$, can be parameterized in different ways. The simplest option is a constant, isotropic intrinsic dispersion, $\sigma(x_{\text{gal}}, y_{\text{gal}}, z_{\text{gal}}) = \sigma_0$, but other possible options include parameterizations $\sigma(R_{\text{gal}})$ based on the surface density of the galactic disk.

For thick disks, as commonly seen in high-redshift galaxies, part of the total dynamical support is from pressure support, and not just from rotation. Thus, the rotation velocity of such a galaxy is lower than the circular velocity, as a result of asymmetric drift. We describe the rotation velocity of our system, with asymmetric drift included, following the formulation of Burkert et al. (2010), derived for a self-gravitating exponential disk and constant dispersion σ_0 :

$$v_{\text{rot}}^2(R_{\text{gal}}) = v_{\text{circ,tot}}^2(R_{\text{gal}}) - 2\sigma_0^2 \left(\frac{R_{\text{gal}}}{r_d} \right) \quad (\text{A4})$$

where r_d is the disk scale radius, and $r_d = R_e/1.68$ for an exponential disk. If we follow the derivation by Burkert et al. (2010), but assume the self-gravitating disk follows a more general Sérsic distribution, the asymmetric drift correction is then

$$v_{\text{rot}}^2(R_{\text{gal}}) = v_{\text{circ,tot}}^2(R_{\text{gal}}) - 2\sigma_0^2 \left(\frac{b_{n_S}}{n_S} \right) \left(\frac{R_{\text{gal}}}{R_e} \right)^{1/n_S}, \quad (\text{A5})$$

where $2(b_{n_S}/n_S) = 3.36$ for an exponential disk ($n_S = 1$). Even more generally, assuming the dispersion is constant with radius R_{gal} (but not necessarily with height z above the midplane), then the asymmetric drift correction is given by Eq. 3 of Burkert et al. (2010) (with a correction term of $\sigma_0^2(d \ln \rho / d \ln r)$, where $r = R_{\text{gal}}$).

A radial motion component can be imprinted on top of the galaxy rotational motion, $\vec{v}_{\text{radial motion}}(x_{\text{gal}}, y_{\text{gal}}, z_{\text{gal}})$. One option is to assume a constant radial flow, defined as $\vec{v}_{\text{radial motion}}(x_{\text{gal}}, y_{\text{gal}}, z_{\text{gal}}) = -v_r \hat{r}_{\text{gal}}$ (where $r_{\text{gal}}^2 = R_{\text{gal}}^2 + z_{\text{gal}}^2$ is the 3D radius of the galaxy, and positive v_r corresponds to inflows), but profiles that vary with radius or azimuthal angle could also be implemented in the future. In the simplest case, we assume this is a perturbation on the other motions, so this motion component follows the light distribution and geometry of the galaxy.

In addition, a detailed biconical outflow model similar to the one described in Bae & Woo (2016) is implemented. For this model component, the light and kinematics follow two axisymmetric cones that share an apex at the location where the outflow is launched, $(x_{\text{out},0}, y_{\text{out},0})$. The shape of the cones are primarily defined by two opening angles, θ_{inner} and θ_{outer} , which delineate the walls of the cones. Each opening angle is measured from the outflow axis such that 0° is along the outflow axis. Only regions between θ_{inner} and θ_{outer} then produce

line emission and affect the line-of-sight (LOS) kinematics. Finally, the cones have a maximum radial extent out to r_{end} .

Relative to the plane of the sky, the cones have an inclination, i_{out} , and position angle PA_{out} that can be different from the galaxy. i_{out} is defined such that 0° indicates an outflow axis along the LOS. The transformation from the sky coordinates $(x_{\text{sky}}, y_{\text{sky}}, z_{\text{sky}})$ back to the intrinsic outflow coordinates $(x_{\text{out}}, y_{\text{out}}, z_{\text{out}})$ is then exactly the same as in Equation A1 except with the specific outflow central coordinate, inclination, and PA.

Three choices of outflow velocity radial profiles are possible: ‘increasing’, ‘decreasing’, or ‘both’. Each of these is parameterized in the following way:

$$\begin{aligned} \text{Increasing : } v_{\text{out}}(r) &= v_{\text{max}} \left(\frac{r}{r_{\text{end}}} \right)^n \\ \text{Decreasing : } v_{\text{out}}(r) &= v_{\text{max}} \left[1 - \left(\frac{r}{r_{\text{end}}} \right)^n \right] \\ \text{Both : } v_{\text{out}}(r) &= \begin{cases} v_{\text{max}} \left(\frac{r}{r_{\text{turn}}} \right)^n, & r < r_{\text{turn}} \\ v_{\text{max}} \left(2 - \frac{r}{r_{\text{turn}}} \right)^n, & r > r_{\text{turn}} \end{cases} \end{aligned} \quad (\text{A6})$$

where n is the power law index of the radial profile, v_{max} defines the maximum velocity that occurs at $r = r_{\text{end}}$ for ‘increasing’, $r = 0$ for ‘decreasing’, and $r = r_{\text{turn}}$ for ‘both’. A velocity dispersion profile $\sigma_{\text{out},0}(r)$ can be chosen for the outflowing gas in the same way as for the galaxy mass components.

Next, the LOS velocity and dispersion cubes are constructed, and sampled over the sky coordinate frame. For the composite rotation velocity profile, the LOS projection factor is $\cos \psi \sin i = \sin i (y_{\text{gal}}/R_{\text{gal}})$. Similarly, LOS projection is determined for non-isotropic dispersion profiles and outflow or radial motion/inflow components.⁶ The LOS velocity and dispersion cubes are thus:

$$\begin{aligned} V(x_{\text{sky}}, y_{\text{sky}}, z_{\text{sky}}) &= v_{\text{rot}}(R_{\text{gal}}) \left(\frac{y_{\text{gal}}}{R_{\text{gal}}} \right) \sin i \\ &+ \left[v_{\text{radial motion}}(x_{\text{gal}}, y_{\text{gal}}, z_{\text{gal}}) \right]_{\text{LOS}} + V_{\text{sys}} \end{aligned} \quad (\text{A7})$$

$$\sigma(x_{\text{sky}}, y_{\text{sky}}, z_{\text{sky}}) = \left[\sigma(R_{\text{gal}}) \right]_{\text{LOS}}, \quad (\text{A8})$$

where Eq. A1 is used to convert from sky to galaxy coordinates, and V_{sys} is the systemic velocity of the system.

For the biconical outflow component, these cubes are:

$$V_{\text{out}}(x_{\text{sky}}, y_{\text{sky}}, z_{\text{sky}}) = v_{\text{out}}(r_{\text{out}}) \cos i' + V_{\text{sys}} \quad (\text{A9})$$

$$\sigma_{\text{out}}(x_{\text{sky}}, y_{\text{sky}}, z_{\text{sky}}) = \left[\sigma_{\text{out},0}(r_{\text{out}}) \right]_{\text{LOS}}, \quad (\text{A10})$$

⁶ I.e., as $\left[\vec{\sigma}(x_{\text{gal}}, y_{\text{gal}}, z_{\text{gal}}) \cdot \hat{z} \right]$ or $\left[\vec{v}_{\text{radial motion}}(x_{\text{gal}}, y_{\text{gal}}, z_{\text{gal}}) \cdot \hat{z} \right]$.

where $r_{\text{out}} = \sqrt{x_{\text{out}}^2 + y_{\text{out}}^2 + z_{\text{out}}^2}$, and i' in Eq. A9 ranges from $i_{\text{out}} - \theta_{\text{outer}}$ to $i_{\text{out}} + \theta_{\text{outer}}$ depending on the location within the outflow cone.

In order to construct a full model cube $I(x_{\text{sky}}, y_{\text{sky}}, V_{\text{los}})$, the information from the velocity and dispersion cubes $V(x_{\text{sky}}, y_{\text{sky}}, z_{\text{sky}})$ and $\sigma(x_{\text{sky}}, y_{\text{sky}}, z_{\text{sky}})$ must be combined and collapsed along the line of sight (z_{sky}). The composite velocity profile at a fixed position $(x_{\text{sky}}, y_{\text{sky}})$ is the intensity-weighted sum of all kinematic components along the line of sight. This requires parameterization of the light distribution of the galactic system, $f(x_{\text{gal}}, y_{\text{gal}}, z_{\text{gal}})$, transformed to sky coordinates $(x_{\text{sky}}, y_{\text{sky}}, z_{\text{sky}})$ using Eq. A1.

In practice, one option is to assume one (or more) mass component (e.g., the baryonic disk) emits light, with a constant mass-to-light ratio Y . This can be approximated by assuming a 2D Sérsic flux distribution within the galaxy midplane, combined with a Gaussian profile in the z_{gal} direction with a width related to the assumed Sérsic flattening q_0 and the component R_e . In this case, $f(R_{\text{gal}}, z_{\text{gal}}) = \Sigma_0 \exp[-b_{n_S} (R_{\text{gal}}/R_e)^{1/n_S}] \times \exp[-0.5(z_{\text{gal}}/h_z)^2]$, with $h_z = q_0 R_e / 1.177$.

The biconical outflow light distribution exponentially decreases as a function of radius with the following profile and parameterization:

$$f_{\text{out}}(r_{\text{out}}) = A \exp\left(-\frac{\tau r_{\text{out}}}{r_{\text{end}}}\right) \quad (\text{A11})$$

where A is the flux at $r_{\text{out}} = 0$, and τ controls the rate at which the flux declines.

The intensity-weighted kinematic distribution collapsed along the line of sight is determined by combining the LOS velocity, dispersion, and flux cubes, assuming the profile at each position can be described as a Gaussian in velocity V_{los} of total flux $f(x_{\text{sky}}, y_{\text{sky}}, z_{\text{sky}})$ and dispersion $\sigma(x_{\text{sky}}, y_{\text{sky}}, z_{\text{sky}})$, centered at $V(x_{\text{sky}}, y_{\text{sky}}, z_{\text{sky}})$:

$$\begin{aligned} I_{\text{intr.}}(x_{\text{sky}}, y_{\text{sky}}, V_{\text{los}}) &= \\ &\sum_{z_{\text{sky}}} \left(\frac{f(x_{\text{sky}}, y_{\text{sky}}, z_{\text{sky}})}{\sigma(x_{\text{sky}}, y_{\text{sky}}, z_{\text{sky}}) \sqrt{2\pi}} \times \right. \\ &\quad \left. \exp\left\{ -\frac{[V_{\text{los}} - V(x_{\text{sky}}, y_{\text{sky}}, z_{\text{sky}})]^2}{2\sigma(x_{\text{sky}}, y_{\text{sky}}, z_{\text{sky}})^2} \right\} + \right. \\ &\quad \left. \frac{f_{\text{out}}(x_{\text{sky}}, y_{\text{sky}}, z_{\text{sky}})}{\sigma_{\text{out}}(x_{\text{sky}}, y_{\text{sky}}, z_{\text{sky}}) \sqrt{2\pi}} \times \right. \\ &\quad \left. \exp\left\{ -\frac{[V_{\text{los}} - V_{\text{out}}(x_{\text{sky}}, y_{\text{sky}}, z_{\text{sky}})]^2}{2\sigma_{\text{out}}(x_{\text{sky}}, y_{\text{sky}}, z_{\text{sky}})^2} \right\} \right), \end{aligned} \quad (\text{A12})$$

using the respective light, velocity, and velocity dispersion distributions for the outflow component and the galaxy.⁷

Finally, this intrinsic kinematic model cube is convolved with a spatial point spread function (PSF) and a spectral line spread function (LSF) to directly include the impact of instrumental and observational effects on the kinematic model. Specifically, the convolution is performed with a 3D kernel folding together the spatial PSF and the spectral LSF:

$$I_{\text{mod}}(x_{\text{sky}}, y_{\text{sky}}, V_{\text{los}}) = I_{\text{intr.}}(x_{\text{sky}}, y_{\text{sky}}, V_{\text{los}}) \otimes \left[\text{PSF}(x_{\text{sky}}, y_{\text{sky}}) * \text{LSF}(V_{\text{los}}) \right] \quad (\text{A13})$$

This model cube is the end result of the DYSMAL forward modeling process. The cube can now be used for comparisons and fitting to observed kinematic data, which we discuss in Section A.2.

A.2. Fitting Galaxy Kinematics using DYSMAL Models

The DYSMAL models presented in the previous subsection can be used to fit a wide variety of galaxy mass and kinematic components to a range of observational data.

First, a DYSMAL model set should be selected based on the specific application. For instance, this might be comprised of a disk, bulge, and halo mass components together with an intrinsic velocity dispersion profile, or it may include a galaxy disk together with an outflow component. The parameters of each of these model components are then set to a fixed value (e.g., fixed bulge-to-total ratio, B/T), allowed to vary as free fit parameters (e.g., free total mass), or are determined as a function of some other parameter (e.g., fitting directly for $f_{\text{DM}}(R_e)$, and then using this to find the halo mass for a NFW profile; alternatively, setting the halo mass from the total baryonic mass, using a fixed f_{gas} and a particular stellar mass-halo mass relation).

Next, depending on the type of observational data, extractions may need to be made from the DYSMAL model cubes. If the observations are to be fit in 3D, using IFS cubes, then the 3D mock DYSMAL cubes are directly comparable to the data. Alternatively, the models can be used to fit 2D extracted kinematic maps or 1D extracted kinematic profiles (or slit observations), for instance fitting both velocity V and dispersion σ simultaneously (though other possibilities are to fit only V , or to fit all of V , σ , and the flux distribution). This is accomplished by applying the same extraction methodology used for the observations on the mock cubes (e.g., Gaussian-fit extractions to 2D velocity and dispersion maps; or flared or straight slit aperture extraction to 1D profiles).

We stress that all observational effects (including beam-smearing, the instrumental line spread function, and any extraction from 3D) are directly included in the resulting

1D/2D/3D DYSMAL models. The full forward modeling of this procedure therefore allows us to directly fit for the intrinsic model properties.

In `DysmalPy`, fitting can be performed either with Markov Chain Monte Carlo (MCMC) parameter space exploration (using `emcee`; Foreman-Mackey et al. 2013) or least-squares fitting (using `MPFIT`; Markwardt 2009). For MCMC fitting with `emcee`, priors $\log p(\theta_i)$ are first selected for each free parameter θ_i in the DYSMAL model; options include flat or Gaussian priors (either bounded or unbounded). The likelihood function for our model is defined to be a Gaussian distribution. For 3D fitting,

$$\log \mathcal{L} = -0.5 \left(\frac{1}{f} \right) \sum_{x_{\text{sky}}, y_{\text{sky}}, V_{\text{los}}} m(x_{\text{sky}}, y_{\text{sky}}, V_{\text{los}}) \times \left\{ \left[\frac{I_{\text{obs}}(x_{\text{sky}}, y_{\text{sky}}, V_{\text{los}}) - I_{\text{mod}}(x_{\text{sky}}, y_{\text{sky}}, V_{\text{los}})}{\text{err}_{\text{obs}}(x, y, V) \left[w(x_{\text{sky}}, y_{\text{sky}}, V_{\text{los}}) \right]^{-1/2}} \right]^2 + \log \left[\frac{2\pi \left(\text{err}_{\text{obs}}(x_{\text{sky}}, y_{\text{sky}}, V_{\text{los}}) \right)^2}{w(x_{\text{sky}}, y_{\text{sky}}, V_{\text{los}})} \right] \right\}, \quad (\text{A14})$$

where I_{mod} is from Eq. A13, I_{obs} is the observed 3D cube, $m(x_{\text{sky}}, y_{\text{sky}}, V_{\text{los}})$ is a data mask (e.g., removing bad pixels or low S/N regions), $w(x_{\text{sky}}, y_{\text{sky}}, V_{\text{los}})$ is any weighting to be applied to the cube (e.g., effectively modifying the uncertainties), and f is an optional factor to account for oversampling of the data relative to the spatial and spectral resolution of the data (to approximate the number of independent data points, removing any impact of oversampling on the relative importance of the likelihood and priors). For 2D or 1D fitting,

$$\log \mathcal{L} = -0.5 \left(\frac{1}{f} \right) \times \sum_{\substack{X=V, [\sigma], \\ [\text{flux}]}} \left\{ \sum_i m_i \left[w_i \left(\frac{X_{\text{obs}, i} - X_{\text{mod}, i}}{\text{err}_{X, i}} \right)^2 + \log \left(\frac{2\pi \text{err}_{X, i}^2}{w_i} \right) \right] \right\}, \quad (\text{A15})$$

where X is either the velocity V , dispersion σ , or flux (e.g., 1D profiles along the slit $V(p)$, $\sigma(p)$, $I(p)$, or 2D maps of V , σ and line intensity I), and X_{obs} and X_{mod} are the data and extracted model maps/profiles, respectively. The outer sum over the maps/profiles X includes only the maps/profiles that are being used for fitting (e.g., simultaneously fitting velocity V and dispersion σ ; see discussion above), and the sum over i denotes the sum over all pixels or data points in the maps/profiles. Similar to the 3D log likelihood, m_i is the data mask, w_i is any data weighting (or no weighting, with $w_i = 1$), and f is the optional factor accounting for spatial data oversampling. The log posterior probability is then

⁷ Note that if there is an inflow signature from a separate gas component, this can be added to the model with a separate light distribution and geometry (i.e., not in Eq. A7), similar to the treatment of the outflow component.

$$\log P(\theta|\text{obs}) = \log \mathcal{L}(\text{obs}|\theta) + \log p(\theta) + \text{const}, \quad (\text{A16})$$

with the log likelihood as defined above and taking the prior as the composite of the individual parameter priors, $\log p(\theta) = \sum_i \log p(\theta_i)$.

The ‘‘best-fit’’ parameter values are determined as the maximum a posteriori (MAP) values from the posteriors, with the option to jointly analyze the posteriors of parameters which exhibit degeneracies, to ensure the MAP values correspond to high probability regions of the multidimensional posterior distribution. The upper and lower 1σ uncertainties for each parameter are estimated independently, using the shortest 68% interval of the marginalized posterior (to ensure reasonable uncertainty estimates in cases where the marginalized posterior is peaked near a boundary for the parameter).

Alternatively, fitting can be performed with `MPFIT`, which uses the Levenberg-Marquardt technique to perform least-squares fitting. For the least-squares fitting with `DysmalPy`, we define χ_{kin}^2 that is tailored to the data dimensionality. For 3D fitting,

$$\chi_{\text{kin}}^2 = \sum_{x_{\text{sky}}, y_{\text{sky}}, V_{\text{los}}} m(x_{\text{sky}}, y_{\text{sky}}, V_{\text{los}}) w(x_{\text{sky}}, y_{\text{sky}}, V_{\text{los}}) \times \left[\frac{I_{\text{obs}}(x_{\text{sky}}, y_{\text{sky}}, V_{\text{los}}) - I_{\text{mod}}(x_{\text{sky}}, y_{\text{sky}}, V_{\text{los}})}{\text{err}_{I_{\text{obs}}(x_{\text{sky}}, y_{\text{sky}}, V_{\text{los}})}} \right]^2 \quad (\text{A17})$$

where as before, I_{obs} and I_{mod} are the observed and model 3D cubes, respectively, $m(x_{\text{sky}}, y_{\text{sky}}, V_{\text{los}})$ is a mask based on the data (e.g., removing bad pixels or low S/N regions) and $w(x_{\text{sky}}, y_{\text{sky}}, V_{\text{los}})$ is any weighting to be applied to the cube. For 2D or 1D fitting,

$$\chi_{\text{kin}}^2 = \sum_{X=V, [\sigma], [\text{flux}]} \left[\sum_i m_i w_i \left(\frac{X_{\text{obs},i} - X_{\text{mod},i}}{\text{err}_{X,i}} \right)^2 \right], \quad (\text{A18})$$

where again X_{obs} and X_{mod} are the observed and model velocity, dispersion or flux maps/profiles (e.g., the observed $V(p)$, $\sigma(p)$, and flux $I(p)$ along the slit for 1D profiles), the outer sum only includes the observed maps/profiles used for simultaneous fitting (e.g., both V and σ , or all of V , σ , and the flux distribution), and m_i and w_i are the data mask and any weighting of the data, respectively.

The best-fit parameter values are then taken directly from the least-squares minimization solution. One approach to derive uncertainties for the least-squares fitting is to then sample the value of χ_{kin}^2 over a grid of values for all free parameters, and use this to determine the uncertainty intervals. However, in practice it is often more computationally efficient to estimate the uncertainties through an accompanying MCMC exploration of the posterior distribution.

A.3. Importance of Prior Choice in MCMC Fitting

While MCMC fitting provides a number of benefits (e.g., simultaneously enabling uncertainty estimation), it is crucial to consider how the choice of priors impacts the sampled posterior distribution. In MCMC sampling, priors can help to restrict fits with degeneracies by applying constraints from ancillary information or physical feasibility (e.g., through bounding and/or the application of Gaussian priors), so that the posterior distribution reflects both the likelihood from the data and these prior constraints. Parameter priors can also be uniform, so the posterior is driven by the likelihood function. However, even adopting uniform priors is a choice that impacts later analysis, because the sampled posterior distribution also depends on how the fit was *parameterized*.⁸

The impact of priors is particularly important when analyzing parameters *inferred* from the fit values. While not fit directly, there is an ‘‘effective prior’’ imprinted on the distribution of sample values for these derived parameters. This ‘‘effective prior’’ is determined by the choice of free fit parameters and their chosen priors (even uniform priors), and depends on the relationship between the fit and derived parameters. Formally, this is simply a change of variables in a probability distribution function (pdf), going from the fit parameter’s prior pdf to a transformed pdf. If x and y are related through $y = f(x)$ and x is fit with a uniform, bounded prior, then as the total probability must be conserved,⁹ the effective prior on y will be proportional to $\left| \frac{d}{dy} [f^{-1}(y)] \right|$, where f^{-1} is the inverse function (Casella & Berger 2002, Eq. 2.1.10).¹⁰

The issue of free parameter and prior selection can have a large impact when fitting galaxy kinematics using MCMC sampling with `DysmalPy`. For example, for a fit with a baryonic component and a NFW halo, if $\log_{10}(M_{\text{vir}}/M_{\odot})$ is chosen as the free parameter with a flat prior, then the distribution of $f_{\text{DM}}(R_e) = v_{\text{DM}}^2(R_e)/v_{\text{circ}}^2(R_e)$ for the MCMC sampling (calculated as ‘‘blobs’’ from the `emcee` sampler) will often diverge towards 0 and 1. This arises in part because a flat prior on $\log_{10}(M_{\text{vir}}/M_{\odot})$ is equivalent to a prior for $f_{\text{DM}}(R_e)$ that diverges as $f_{\text{DM}}(R_e) \rightarrow 0$, or $f_{\text{DM}}(R_e) \rightarrow 1$, because sampling uniformly from the $\log_{10}(M_{\text{vir}}/M_{\odot})$ prior produces a pile-up of $\log_{10}(M_{\text{vir}}/M_{\odot})$ values that all map to similarly small/large values of $f_{\text{DM}}(R_e)$. If $f_{\text{DM}}(R_e)$ is fairly poorly constrained by the data (i.e., a shallow likelihood function), the effective probability distribution for $f_{\text{DM}}(R_e)$ will thus primarily reflect this ‘‘effective,’’ diverging prior.

⁸ For further discussion on the impact of parameter transformations on probability (i.e., prior and posterior) distributions, see Sivia & Skilling (2006), Hogg (2012), and Hogg & Foreman-Mackey (2018).

⁹ I.e., $\int_a^b p_X(x) dx = \int_{f(a)}^{f(b)} p_Y(y) dy$

¹⁰ More generally, for a prior pdf $p_X(x)$ for x , the transformed prior pdf for $y = f(x)$ is $p_Y(y) = p_X(f^{-1}(y)) \left| \frac{d}{dy} [f^{-1}(y)] \right|$, assuming ‘‘well-behaved’’ functions (i.e., $p_X(x)$ is continuous and normalizable, and $f^{-1}(y)$ is continuously differentiable; Casella & Berger 2002, Sec 2.1, Theorem 2.1.5).

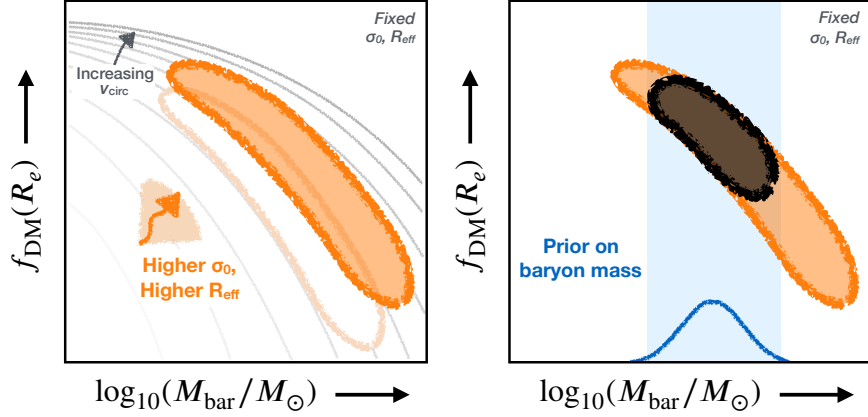


Figure 7. Illustration of how the velocity dispersion and disk radius, and the prior on the baryonic mass, can impact the degeneracy between a galaxy’s total baryonic mass and its dark matter fraction. There tends to be an anti-correlation between $f_{\text{DM}}(R_e)$ and $\log_{10}(M_{\text{bar}}/M_{\odot})$ at constant σ_0 and $R_{e,\text{disk}}$, roughly tracing lines of constant v_{circ} (i.e., total dynamical mass). (Left panel) If the dispersion or disk radius is increased, then the likelihood degeneracy region shifts towards higher $f_{\text{DM}}(R_e)$ and higher $\log_{10}(M_{\text{bar}}/M_{\odot})$ (as illustrated in the left panel). The exact direction and magnitude of the shifts depend on the detailed model values, but in general a higher v_{circ} is needed to counterbalance the increased asymmetric drift correction or stretched rotation curve (for σ_0 and $R_{e,\text{disk}}$, respectively). (Right panel) For a given fixed σ_0 and $R_{e,\text{disk}}$, by applying a Gaussian prior on the baryonic mass, the posterior $f_{\text{DM}}(R_e)$ – $\log_{10}(M_{\text{bar}}/M_{\odot})$ degeneracy (dark blue region, right panel) will be modified relative to the likelihood degeneracy (purple region).

Therefore, if the aim is to measure $f_{\text{DM}}(R_e)$ rather than $\log_{10}(M_{\text{vir}}/M_{\odot})$, it is better to fit directly for $f_{\text{DM}}(R_e)$. For this inverted parameterization, the choice of a flat prior for $f_{\text{DM}}(R_e)$ corresponds to an effective prior on $\log_{10}(M_{\text{vir}}/M_{\odot})$ that is a peaked distribution (i.e., essentially the inverse of the opposite case that diverges towards the bounds). Because of this parameterization and prior choice issue, in this paper we chose to fit directly for $f_{\text{DM}}(R_e)$, as this is the quantity of interest.

A.4. DYSMAL Parameter Fitting Degeneracies for RC41 Curves and the Impact of Priors

Fitting the kinematics of high-redshift galaxies with mass and kinematic models — such as with DYSMAL — is complicated by degeneracies between different components. These degeneracies arise in part from the impact of beam smearing, given the relatively low spatial resolution of the observations, and from relatively modest S/N of the data, even for very deep observations such as our RC41 sample. At lower S/N and lower spatial resolution, it can be difficult to disentangle the velocity signatures of a bulge, thick disk, and halo, as profile differences can be smoothed out to the point where they cannot be distinguished within the observational uncertainties.¹¹ Thus, while the lower halo concentrations at higher redshifts should help to break the disk-halo degeneracy that is observed in local galaxies (see the discussion in Paper I), the relatively limited spatial resolution and S/N of our observations compared to what is currently achievable for

local galaxies tends to produce a similar baryon-halo degeneracy.

When modeling our galaxies with a bulge, a thick disk, a NFW halo, and a constant intrinsic velocity dispersion (with free parameters $\log_{10}(M_{\text{bar}}/M_{\odot})$, $f_{\text{DM}}(R_e)$, $R_{e,\text{disk}}$, and σ_0), we tend to find an anti-correlation between the total baryonic mass and the dark matter fractions. This degeneracy is not unexpected, as it roughly traces lines of constant v_{circ} , reflecting a trade-off between dark and baryonic matter that is accentuated by the smoothing of the different velocity curve shapes by the effects of beam smearing (i.e., the total mass is better constrained than the mass partitioning). However, the exact position and shape of this degeneracy depends on the values of other model parameters, particularly the intrinsic velocity dispersion σ_0 and the disk effective radius, $R_{e,\text{disk}}$.

The values of σ_0 and $R_{e,\text{disk}}$ are connected to the dark matter fraction–baryonic mass degeneracy through the asymmetric drift correction (see Sec. 6.2) and both the definition $f_{\text{DM}}(R_e \equiv R_{e,\text{disk}})$ and the role of $R_{e,\text{disk}}$ in setting the model rotation curve profile, respectively. In general, increasing both σ_0 and $R_{e,\text{disk}}$ results in shifting the region of highest $f_{\text{DM}}(R_e)$ – $\log_{10}(M_{\text{bar}}/M_{\odot})$ likelihood towards lines of higher v_{circ} , as illustrated in the left panel of Figure 7. Increasing σ_0 leads to larger asymmetric drift corrections, or lower v_{rot} for a fixed model v_{circ} (i.e., fixed total mass). Matching the observed v_{rot} thus requires increasing v_{circ} . When increasing $R_{e,\text{disk}}$, the intrinsic rotation curve profile is stretched to peak/flatten at larger radii, without impacting the maximum rotation velocity. Therefore, to match the inner rising profile of the observed $v_{\text{rot}}(r)$, the total mass must also be increased (i.e., higher model v_{circ}). The exact position and extent of this degeneracy is more complex than this fixed-value illustration, as all four parameters ($\log_{10}(M_{\text{bar}}/M_{\odot})$, $f_{\text{DM}}(R_e)$, $R_{e,\text{disk}}$, σ_0) are free. Nonetheless, this simplified

¹¹ We note that while we focus here on how these issues impact parametric kinematic modeling, these resolution and S/N limitations of the data also complicate constraints of galaxy kinematics using nonparametric methods.

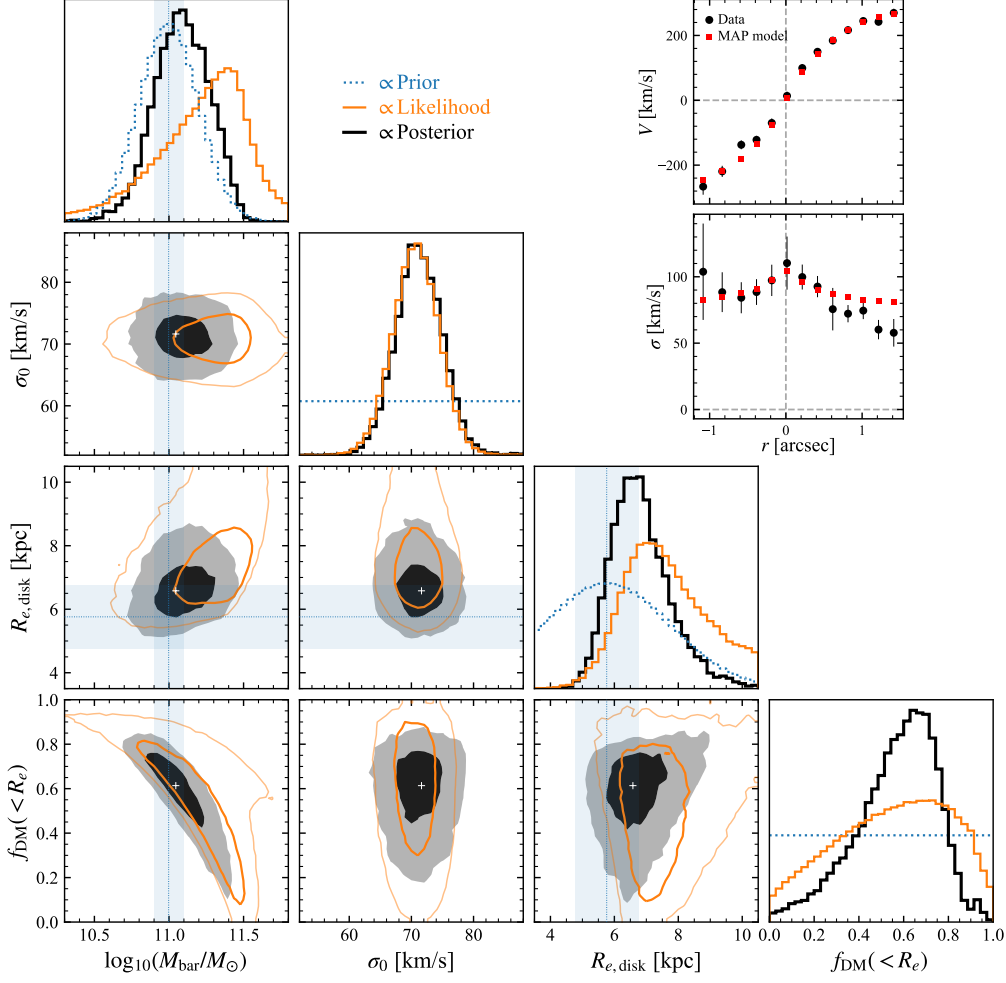


Figure 8. Comparison of the marginalized prior, posterior, and approximate likelihood contours for the free parameters in the 1D fitting for one galaxy in our sample (BX482). The normalized priors for each parameter are shown in the histogram panels (diagonal) as blue dotted curves. For Gaussian priors, the center and standard deviation are marked with vertical/horizontal blue lines and shaded regions, respectively. The marginalized approximate likelihood and posterior distributions are shown in orange and black/grey, respectively, with the 1 and 2 σ intervals denoted with the 2D contours (with a 2D Gaussian filter of standard deviation 0.5 bins applied for clarity). The Gaussian priors on $\log_{10}(M_{\text{bar}}/M_{\odot})$ and $R_{e,\text{disk}}$ impact the peak and broadness of the posterior distribution for both parameters, and additionally contribute to a narrower $f_{\text{DM}}(R_e) - \log_{10}(M_{\text{bar}}/M_{\odot})$ degeneracy, both along the anti-correlation ($\log_{10}(M_{\text{bar}}/M_{\odot})$) and perpendicular to it ($R_{e,\text{disk}}$). The *maximum a posteriori* (MAP) values of each parameter (found by joint posterior analysis) are shown with white plus signs. We also show the 1D observed $V(r)$ and $\sigma(r)$ curves along with the 1D-extracted MAP model (black circles, red squares, respectively) in the upper-right inset panels.

picture helps to understand the likelihood degeneracy for the full fit, as a range of σ_0 or $R_{e,\text{disk}}$ values will contribute to a broadening of the degeneracy region (i.e., spanning more values of v_{circ}), roughly corresponding to overlapping regions of fixed σ_0 and $R_{e,\text{disk}}$.

The final posterior degeneracy between $f_{\text{DM}}(R_e)$ and $\log_{10}(M_{\text{bar}}/M_{\odot})$ depends not only on the likelihood degeneracy, but also on the Gaussian priors on $\log_{10}(M_{\text{bar}}/M_{\odot})$ and $R_{e,\text{disk}}$. In the limit where the data are not highly informative, the Gaussian priors will help to restrict the posteriors of these parameters to narrower ranges. Thus, the $\log_{10}(M_{\text{bar}}/M_{\odot})$ prior will help break the $f_{\text{DM}}(R_e) - \log_{10}(M_{\text{bar}}/M_{\odot})$ degeneracy by “picking out” a subsection of the $\log_{10}(M_{\text{bar}}/M_{\odot})$ val-

ues covered (see Figure 7, right panel). The $R_{e,\text{disk}}$ prior will also have an impact, since a narrowing of the $R_{e,\text{disk}}$ parameter space will translate to narrowing of the diagonal shift of the $f_{\text{DM}}(R_e) - \log_{10}(M_{\text{bar}}/M_{\odot})$ anti-correlation (effectively, fewer overlapping degeneracy regions, as fewer $R_{e,\text{disk}}$ values are highly probable).

To illustrate the parameter degeneracies and the role of the priors, in Figure 8 we show the prior, likelihood, and posterior distributions in all 1D and 2D projected spaces for one galaxy in our sample (BX482). The posterior distribution (black lines and black/grey filled regions) is determined from the 1D MCMC sampler chain, and the likelihood distribution (orange lines and contours) is approximated by performing a

separate MCMC sampling with uninformative (i.e., bounded flat) priors for all parameters.¹² The 1D priors are shown with dotted blue lines, and the center and standard deviation of the Gaussian priors on $\log_{10}(M_{\text{bar}}/M_{\odot})$ and $R_{e,\text{disk}}$ are marked with blue lines and shaded regions in the projected 1D and 2D panels, and the 1D histograms are all normalized, as the correct scaling factors have not been determined.

The impact of the Gaussian priors on $\log_{10}(M_{\text{bar}}/M_{\odot})$ and $R_{e,\text{disk}}$ can be seen in both the 1D and 2D histograms, as the posterior peaks for these parameters lie between the prior and likelihood peaks (as do the MAP values, which are found by jointly analyzing all free parameters; white plus signs), and the marginalized posterior distribution peaks are less broad than those of the likelihood. Because of the

$f_{\text{DM}}(R_e) - \log_{10}(M_{\text{bar}}/M_{\odot})$ degeneracy (bottom left panel), the $\log_{10}(M_{\text{bar}}/M_{\odot})$ prior also impacts the posterior distribution of $f_{\text{DM}}(R_e)$, and yields a narrower posterior degeneracy than for the likelihood distribution. The restriction of the $R_{e,\text{disk}}$ values from the prior also contributes to narrowing of the degeneracy region, but in the direction perpendicular to the anti-correlation (i.e., spanning a narrower range of constant v_{circ} ; see Figure 7). Although the actual posterior probability distributions for each galaxy will also depend on other model parameters and on the peculiarities of the observed rotation and dispersion curves, the trends discussed here account for the overall qualitative properties of the posteriors determined from our MCMC analysis of the RC41 sample.

REFERENCES

- Astropy Collaboration, Robitaille, T. P., Tollerud, E. J., et al. 2013, *A&A*, 558, A33
- Astropy Collaboration, Price-Whelan, A. M., Sipőcz, B. M., et al. 2018, *AJ*, 156, 123
- Bae, H.-J., & Woo, J.-H. 2016, *ApJ*, 828, 97
- Binney, J., & Tremaine, S. 2008, *Galactic Dynamics: Second Edition*, 2nd edn. (Princeton, NJ, USA: Princeton University Press)
- Bouché, N., Carfantan, H., Schroetter, I., Michel-Dansac, L., & Contini, T. 2015, *AJ*, 150, 92
- Bradley, L., Sipőcz, B., Robitaille, T., et al. 2019, *astropy/photutils: v0.7.2*, v0.7.2, Zenodo, doi:10.5281/zenodo.3568287
- . 2020, *astropy/photutils: 1.0.1*, v1.0.1, Zenodo, doi:10.5281/zenodo.4049061
- Bullock, J. S., Kolatt, T. S., Sigad, Y., et al. 2001, *MNRAS*, 321, 559
- Burkert, A. 1995, *ApJ*, 447, L25
- Burkert, A., Genzel, R., Bouché, N., et al. 2010, *ApJ*, 725, 2324
- Carignan, C., & Freeman, K. C. 1985, *ApJ*, 294, 494
- Casella, G., & Berger, R. 2002, *Statistical Inference*, 2nd edn., Duxbury Advanced Series in Statistics and Decision Sciences (Pacific Grove, CA, USA: Thomson Learning)
- Casertano, S. 1983, *MNRAS*, 203, 735
- Chabrier, G. 2003, *PASP*, 115, 763
- Cole, D. R., Dehnen, W., & Wilkinson, M. I. 2011, *MNRAS*, 416, 1118
- Courteau, S., & Dutton, A. A. 2015, *ApJL*, 801, L20
- Courteau, S., Cappellari, M., de Jong, R., et al. 2014, *Rev Modern Phys*, 86, 47
- Cresci, G., Hicks, E. K. S., Genzel, R., et al. 2009, *ApJ*, 697, 115
- Davies, R., Förster Schreiber, N. M., Cresci, G., et al. 2011, *ApJ*, 741, 69
- Dekel, A., Ishai, G., Dutton, A. A., & Maccio, A. V. 2017, *MNRAS*, 468, 1005
- Dekel, A., & Silk, J. 1986, *ApJ*, 303, 39
- Di Teodoro, E. M., & Fraternali, F. 2015, *MNRAS*, 451, 3021
- Drew, P. M., Casey, C. M., Burnham, A. D., et al. 2018, *ApJ*, 869, 58
- Dutton, A. A., & Macciò, A. V. 2014, *MNRAS*, 441, 3359
- Einasto, J. 1965, *Trudy Inst. Astrofiz. Alma-Ata*, 5, 87
- El-Zant, A., Shlosman, I., & Hoffman, Y. 2001, *ApJ*, 560, 636
- Erb, D. K., Steidel, C. C., Shapley, A. E., et al. 2006, *ApJ*, 646, 107
- Foreman-Mackey, D. 2016, *The Journal of Open Source Software*, 1, 24
- Foreman-Mackey, D., Hogg, D. W., Lang, D., & Goodman, J. 2013, *PASP*, 125, 306
- Förster Schreiber, N. M., & Wuyts, S. 2020, *ARA&A*, 58, 661
- Förster Schreiber, N. M., Genzel, R., Lehnert, M. D., et al. 2006, *ApJ*, 645, 17
- Förster Schreiber, N. M., Genzel, R., Bouché, N., et al. 2009, *ApJ*, 706, 1364
- Förster Schreiber, N. M., Genzel, R., Newman, S. F., et al. 2014, *ApJ*, 787, 38
- Förster Schreiber, N. M., Renzini, A., Mancini, C., et al. 2018, *ApJS*, 238, 21
- Freeman, K. C. 1970, *ApJ*, 160, 811
- Freundlich, J., Dekel, A., Jiang, F., et al. 2020, *MNRAS*, 491, 4523
- Freundlich, J., Combes, F., Tacconi, L. J., et al. 2019, *A&A*, 622, 1
- Genzel, R., Tacconi, L. J., Eisenhauer, F., et al. 2006, *Nature*, 442, 786
- Genzel, R., Burkert, A., Bouché, N., et al. 2008, *ApJ*, 687, 59
- Genzel, R., Newman, S., Jones, T., et al. 2011, *ApJ*, 733, 101
- Genzel, R., Tacconi, L. J., Kurk, J., et al. 2013, *ApJ*, 773, 68
- Genzel, R., Förster Schreiber, N. M., Lang, P., et al. 2014, *ApJ*, 785, 75
- Genzel, R., Förster Schreiber, N. M., Übler, H., et al. 2017, *Nature*, 543, 397
- Genzel, R., Price, S. H., Übler, H., et al. 2020, *ApJ*, 902, 98
- Goerdt, T., Moore, B., Read, J. I., & Stadel, J. 2010, *ApJ*, 725, 1707
- Harris, C. R., Millman, K. J., van der Walt, S. J., et al. 2020, *Nature*, 585, 357
- Hogg, D. W. 2012, arXiv:1205.4446
- Hogg, D. W., & Foreman-Mackey, D. 2018, *ApJS*, 236, 11
- Hunter, J. D. 2007, *Computing in Science & Engineering*, 9, 90
- Johansson, P. H., Naab, T., & Ostriker, J. P. 2009, *ApJL*, 697, L38
- Lang, P., Förster Schreiber, N. M., Genzel, R., et al. 2017, *ApJ*, 840, 92
- Lovell, M. R., Pillepich, A., Genel, S., et al. 2018, *MNRAS*, 481, 1950
- Ludlow, A. D., Navarro, J. F., Angulo, R. E., et al. 2014, *MNRAS*, 441, 378
- Markwardt, C. B. 2009, in *Astronomical Society of the Pacific Conference Series*, Vol. 411, *Astronomical Data Analysis Software and Systems XVIII*, ed. D. A. Bohlender, D. Durand, & P. Dowler, 251
- Martizzi, D., Teyssier, R., & Moore, B. 2013, *MNRAS*, 432, 1947
- Mashchenko, S., Wadsley, J., & Couchman, H. M. 2008, *Science*, 319, 174
- McKinney, W. 2010, in *Proceedings of the 9th Python in Science Conference*, ed. Stéfan van der Walt & Jarrod Millman, 56 – 61
- Mo, H. J., & Mao, S. 2004, *MNRAS*, 353, 829
- Molina, J., Ibar, E., Smail, I., et al. 2019, *MNRAS*, 487, 4856
- Moore, B. P., Naab, T., & White, S. D. M. 2020, *MNRAS*, 499, 4748
- Navarro, J. F., Frenk, C. S., & White, S. D. M. 1996, *ApJ*, 462, 563
- Nipoti, C., & Binney, J. 2015, *MNRAS*, 446, 1820
- Noordermeer, E. 2008, *MNRAS*, 385, 1359
- Orkney, M. D. A., Read, J. I., Rey, M. P., et al. 2021, arXiv:2101.02688
- Pérez, F., & Granger, B. E. 2007, *Computing in Science and Engineering*, 9, 21
- Pontzen, A., & Governato, F. 2012, *MNRAS*, 421, 3464
- . 2014, *Nature*, 506, 171
- Price, S. H., Kriek, M., Shapley, A. E., et al. 2016, *ApJ*, 819, 80
- Price, S. H., Kriek, M., Barro, G., et al. 2020, *ApJ*, 894, 91
- Read, J. I., & Gilmore, G. 2005, *MNRAS*, 356, 107
- Romano-Díaz, E., Shlosman, I., Heller, C., & Hoffman, Y. 2009, *ApJ*, 702, 1250
- Rubin, V. C., & Ford, W. Kent, J. 1970, *ApJ*, 159, 379
- Sivia, D. S., & Skilling, J. 2006, *Data Analysis - A Bayesian Tutorial*, 2nd edn., Oxford Science Publications (Oxford University Press)

¹² Technically, this gives a posterior distribution that is directly proportional to the likelihood. However, as we are concerned with relative distributions for this illustration, this is an acceptable approximation. See Hogg & Foreman-Mackey (2018) for an in-depth discussion on MCMC sampling and prior, likelihood, and posterior distributions.

- Speagle, J. S., Steinhardt, C. L., Capak, P. L., & Silverman, J. D. 2014, *ApJS*, 214, 15
- Tacconi, L. J., Genzel, R., & Sternberg, A. 2020, *ARA&A*, 58, 157
- Tacconi, L. J., Neri, R., Genzel, R., et al. 2013, *ApJ*, 768, 74
- Tacconi, L. J., Genzel, R., Saintonge, A., et al. 2018, *ApJ*, 853, 179
- Teklu, A. F., Remus, R.-S., Dolag, K., et al. 2018, *ApJL*, 854, L28
- The pandas development team. 2020, pandas-dev/pandas, Zenodo, doi:10.5281/zenodo.3509134
- Tiley, A. L., Swinbank, A. M., Harrison, C. M., et al. 2019, *MNRAS*, 485, 934
- Übler, H., Förster Schreiber, N. M., Genzel, R., et al. 2017, *ApJ*, 842, 121
- Übler, H., Genzel, R., Tacconi, L. J., et al. 2018, *ApJL*, 854, L24
- Übler, H., Genel, S., Sternberg, A., et al. 2021, *MNRAS*, 500, 4597
- van Albada, T. S., Bahcall, J. N., Begeman, K., & Sancisi, R. 1985, *ApJ*, 295, 305
- van der Kruit, P., & Freeman, K. 2011, *ARA&A*, 49, 301
- van der Kruit, P. C., & Allen, R. J. 1978, *ARA&A*, 16, 103
- Van Der Walt, S., Colbert, S. C., & Varoquaux, G. 2011, *Computing in Science & Engineering*, 13, 22
- van der Wel, A., Franx, M., van Dokkum, P. G., et al. 2014, *ApJ*, 788, 28
- van Dokkum, P. G., Nelson, E. J., Franx, M., et al. 2015, *ApJ*, 813, 23
- Virtanen, P., Gommers, R., Oliphant, T. E., et al. 2020, *Nature Methods*, 17, 261
- Weinberg, M. D., & Katz, N. 2007, *MNRAS*, 375, 460
- Whitaker, K. E., Franx, M., Leja, J., et al. 2014, *ApJ*, 795, 104
- Wuyts, S., Förster Schreiber, N. M., Wisnioski, E., et al. 2016, *ApJ*, 831, 149
- Zolotov, A., Dekel, A., Mandelker, N., et al. 2015, *MNRAS*, 450, 2327